Gemini planet imager spectroscopy of the dusty substellar companion HD 206893 B

Ward Duong, K.; Patience, J.; Follette, K.; De Rosa, R.J.; Rameau, J.; Marley, M.; … ; Wolff, S.G.

Note: To cite this publication please use the final published version (if applicable).

Gemini Planet Imager Spectroscopy of the Dusty Substellar Companion HD 206893 B

K. Ward-Duong,[1,2] J. Patience,[2] K. Follette,[3] R. J. De Rosa,[4,5] J. Rameau,[6,7] M. Marley,[8] D. Saumon,[9] E. L. Nielsen,[4]
A. Rajan,[10] A. Z. Greenbaum,[11] J. Lee,[12] J. J. Wang,[13,14,*] I. Czekala,[14,15,†] G. Duchêne,[14,6] B. Macintosh,[15]
S. Mark Ammons,[16] V. P. Bailey,[17] T. Barman,[18] J. Bulger,[19,20] C. Chen,[21] J. Chilcote,[15,22] T. Cotten,[23] R. Doyon,[7]
T. M. Esposito,[14] M. P. Fitzgerald,[24] B. L. Gerard,[25,26] S. J. Goodsell,[27] J. R. Graham,[14] P. Hibon,[5] J. Hom,[2]
L.-W. Hung,[28] P. Ingraham,[29] P. Kalas,[14,30] Q. Konopacky,[31] J. E. Larkin,[24] J. Maire,[31] F. Marchis,[30] C. Marois,[26,32]
S. Metchev,[33,34] M. A. Millar-Blanchaer,[17,35] R. Oppenheimer,[36] D. Palmer,[16] M. Perrin,[21] L. Poyneer,[16] L. Pueyo,[21]
F. T. Rantakyrö,[37] B. Ren,[38] J.-B. Ruffio,[15] D. Savransky,[39] A. C. Schneider,[40,41] A. Sivaramakrishnan,[21] I. Song,[23]
R. Soummer,[21] M. Tallis,[15] S. Thomas,[29] J. Kent Wallace,[17] S. Wiktorowicz,[42] and S. Wolff[43]

[1]Five College Astronomy Department, Amherst College, Amherst, MA, 01002
[2]School of Earth and Space Exploration, Arizona State University, P.O. Box 871404, Tempe, AZ 85287, USA
[3]Physics & Astronomy Department, Amherst College, 21 Merrill Science Dr., Amherst, MA 01002
[4]Kavli Institute for Particle Astrophysics and Cosmology, Stanford University, Stanford, CA, USA 94305
[5]European Southern Observatory, Alonso de Córdova 3107, Vitacura, Santiago, Chile
[6]Univ. Grenoble Alpes/CNRS, IPAG, F-38000 Grenoble, France
[7]Institut de Recherche sur les Exoplanètes, Département de Physique, Université de Montréal, Montréal QC, H3C 3J7, Canada
[8]NASA Ames Research Center, Mountain View, CA, USA 94035
[9]Los Alamos National Laboratory, P.O. Box 1663, Los Alamos, NM 87545, USA
[10]Space Telescope Science Institute, Baltimore, MD, USA 21218
[11]Department of Astronomy, University of Michigan, Ann Arbor MI, USA 48109
[12]Department of Physics and Astronomy, University of Georgia, Athens, GA, USA 30602
[13]Department of Astronomy, California Institute of Technology, Pasadena, CA 91125, USA
[14]Department of Astronomy, University of California, Berkeley, CA 94720, USA
[15]Kavli Institute for Particle Astrophysics and Cosmology, Stanford University, Stanford, CA 94305, USA
[16]Lawrence Livermore National Laboratory, Livermore, CA 94551, USA
[17]Jet Propulsion Laboratory, California Institute of Technology, Pasadena, CA 91109, USA
[18]Lunar and Planetary Laboratory, University of Arizona, Tucson AZ 85721, USA
[19]Institute for Astronomy, University of Hawaii, 2680 Woodlawn Drive, Honolulu, HI 96822, USA
[20]Subaru Telescope, NAOJ, 650 North A'ohoku Place, Hilo, HI 96720, USA
[21]Space Telescope Science Institute, Baltimore, MD 21218, USA
[22]Department of Physics, University of Notre Dame, 225 Nieuwland Science Hall, Notre Dame, IN, 46556, USA
[23]Department of Physics and Astronomy, University of Georgia, Athens, GA 30602, USA
[24]Department of Physics & Astronomy, University of California, Los Angeles, CA 90095, USA
[25]Department of Astronomy, UC Santa Cruz, 1156 High St., Santa Cruz, CA 95064, USA
[26]National Research Council of Canada Herzberg, 5071 West Saanich Rd, Victoria, BC, V9E 2E7, Canada
[27]Gemini Observatory, 670 N. A'ohoku Place, Hilo, HI 96720, USA
[28]Natural Sounds and Night Skies Division, National Park Service, Fort Collins, CO 80525, USA
[29]Large Synoptic Survey Telescope, 950N Cherry Ave., Tucson, AZ 85719, USA
[30]SETI Institute, Carl Sagan Center, 189 Bernardo Ave., Mountain View CA 94043, USA
[31]Center for Astrophysics and Space Science, University of California San Diego, La Jolla, CA 92093, USA
[32]University of Victoria, 3800 Finnerty Rd, Victoria, BC, V8P 5C2, Canada
[33]Department of Physics and Astronomy, Centre for Planetary Science and Exploration, The University of Western Ontario, London, ON N6A 3K7, Canada
[34]Department of Physics and Astronomy, Stony Brook University, Stony Brook, NY 11794-3800, USA
[35]NASA Hubble Fellow
[36]Department of Astrophysics, American Museum of Natural History, New York, NY 10024, USA
[37]Gemini Observatory, Casilla 603, La Serena, Chile
[38]Department of Physics and Astronomy, Johns Hopkins University, Baltimore, MD 21218, USA
[39]Sibley School of Mechanical and Aerospace Engineering, Cornell University, Ithaca, NY 14853, USA

Corresponding author: K. Ward-Duong
kwduong@stsci.edu

[40] *US Naval Observatory, Flagstaff Station, P.O. Box 1149, Flagstaff, AZ 86002, USA*

[41] *Department of Physics and Astronomy, George Mason University, MS3F3, 4400 University Drive, Fairfax, VA 22030, USA*

[42] *The Aerospace Corporation, El Segundo, CA 90245, USA*

[43] *Leiden Observatory, Leiden University, P.O. Box 9513, 2300 RA Leiden, The Netherlands*

ABSTRACT

We present new near-infrared Gemini Planet Imager (GPI) spectroscopy of HD 206893 B, a substellar companion orbiting within the debris disk of its F5V star. The *J*, *H*, *K1*, and *K2* spectra from GPI demonstrate the extraordinarily red colors of the object, confirming it as the reddest substellar object observed to date. The significant flux increase throughout the infrared presents a challenging atmosphere to model with existing grids. Best-fit values vary from 1200 K to 1800 K for effective temperature and from 3.0 to 5.0 for $\log(g)$, depending on which individual wavelength band is fit and which model suite is applied. The extreme redness of the companion can be partially reconciled by invoking a high-altitude layer of sub-micron dust particles, similar to dereddening approaches applied to the peculiar red field L-dwarf population. However, reconciling the HD 206893 B spectra with even those of the reddest low-gravity L-dwarf spectra still requires the contribution of additional atmospheric dust, potentially due to the debris disk environment in which the companion resides. Orbit fitting from four years of astrometric monitoring is consistent with a $\sim$30-year period, orbital inclination of 147°, and semimajor axis of 10 au, well within the estimated disk inner radius of $\sim$50 au. As one of very few substellar companions imaged interior to a circumstellar disk, the properties of this system offer important dynamical constraints on companion-disk interaction and provide a benchmark for substellar and planetary atmospheric study.

1. INTRODUCTION

Low-mass directly-imaged companions, ranging from brown dwarfs to extrasolar giant planets, present an ideal laboratory to test formation mechanisms, measure atmospheric properties, and constrain the frequency of companions at large orbital separations. The population of directly-imaged giant planets remains small (see review and recent survey results: Bowler 2016; Galicher et al. 2016; Nielsen et al. 2019), and merits careful comparison with higher-mass brown dwarf companions observed over a wide range of system separations. Together with both free-floating planetary mass objects (e.g., Liu et al. 2013; Gagné et al. 2015; Kellogg et al. 2016; Schneider et al. 2016) and field brown dwarfs (e.g., Burgasser et al. 2006; Kirkpatrick et al. 2011), substellar companions provide more readily characterizable analogs for study and comparison with planetary companions.

Within the brown dwarf population itself, a diversity of spectral features, intrinsic color, and luminosity has been observed. Spectroscopic analysis has shown that objects with the same optical spectral classification may have divergent near-infrared (NIR) colors (Leggett et al. 2003), with younger objects occupying a significantly redder and fainter region of color-magnitude space and systematically cooler effective temperatures (e.g., Filippazzo et al. 2015). NIR color-magnitude analyses of field brown dwarfs, planetary-mass companions, and isolated low-mass, low-gravity objects have demonstrated distinct sequences between the three populations, corresponding to diversity in physical properties across spectral type, gravity, and age. Liu et al. (2016) identified similar photometric properties for late-M to late-L isolated ("free-floating") substellar objects and young bound companions, but with indications that the young field population is brighter and/or redder (even for systems within the same moving groups). With the relative paucity of substellar companions, each discovery provides a unique opportunity for comparison across various classes of substellar objects, contributing useful context that improves our understanding of brown dwarf/planet physical processes, formation pathways, and composition.

Bound substellar companion systems that also host a circumstellar disk provide opportunities to constrain and characterize the orbital properties of low-mass companions and disk-companion dynamical interaction. Studies with high-contrast imaging techniques have now imaged systems with

companions in the region between the warm inner disk (e.g., HR 3549; Mawet et al. 2015) and the inner edge of a substantial outer debris disk (e.g., HR 2562; Konopacky et al. 2016). While directly imaged companions can explain the observed disk morphology for systems like HR 2562, in other cases the presence of additional planets is needed to explain complex disk geometries (e.g., HD 95086; Rameau et al. 2016). Even fewer systems have proven amenable to resolved imaging of both the companion and the disk simultaneously. With marginally-resolved $70\,\mu\text{m}$ *Herschel* PACS imaging, faint disk structure from broad-band SPHERE imaging, and a close substellar companion at 11 au (Milli et al. 2017), the HD 206893 system is among only six systems hosting resolved disks and companions, in addition to β Pictoris (Lagrange et al. 2010), Fomalhaut (Kalas et al. 2008), LkCa 15 (Thalmann et al. 2010; Kraus & Ireland 2012), HD 106906 (Bailey et al. 2014), and PDS 70 (Keppler et al. 2018).

1.1. *HD 206893 System Properties*

Using the Spectro-Polarimetric High-contrast Exoplanet REsearch (SPHERE; Beuzit et al. 2008) instrument on VLT, the SPHERE High Angular Resolution Debris Disc Survey (SHARDDS) discovered a low-mass companion orbiting the F5V star HD 206893 (Milli et al. 2017). The star was initially selected as a target for the SHARDDS resolved debris disk study with the SPHERE/IRDIS instrument (Dohlen et al. 2008) owing to the high fractional IR luminosity of its disk ($L_{dust}/L_* = 2.3 \times 10^{-4}$; Moór et al. 2006), and characterization of the spectral energy distribution (SED) from Chen et al. (2014). After an initial H-band detection of the companion in 2015, subsequent follow-up in 2016 with VLT/NaCo $L^{'}$ imaging using an annular groove phase mask coronagraph (Mawet et al. 2005) recovered the source at $L^{'}$. With a bright $L^{'} = 13.43^{+0.17}_{-0.15}$ magnitude relative to the initial measurement of $H = 16.79 \pm 0.06$, indicating an extremely red color, the object's position in the color-magnitude diagram is analogous to the L5–L9 field dwarf population. With two imaged epochs, Milli et al. (2017) confirmed the comoving nature of the object using an additional non-detection at the expected position of a background object in archival *Hubble Space Telescope*/NICMOS data. Without known association to a moving group, and with literature ages ranging from 0.2–2.1 Gyr (Zuckerman & Song 2004; David & Hillenbrand 2015), companion mass estimates range from 24–73M_{Jup} using the COND models (Baraffe et al. 2003). With SPHERE IFS and IRDIS observations, Delorme et al. (2017) conducted a follow-up study of the system, including revised stellar properties of the primary (estimating solar metallicity and an age from 50–700 Myr), and analysis of $R \sim 30$ YJ spectra (0.95 to 1.64 μm) and 2.11 and 2.25 μm K-band photometry of the companion. These data and analyses substantiated the unusual proper-

ties of the companion, establishing it as the reddest of any currently-known substellar objects, and provided an estimation of its spectral properties as those of a dusty, intermediate gravity L-dwarf.

In addition to the brown dwarf detection, the debris disk of the system was tentatively detected in the widefield IRDIS data, and also marginally resolved in archival *Herschel* 70 μm data. From the *Herschel* imaging, Milli et al. (2017) applied a joint SED and imaging fit to estimate the parameters of the debris disk, reporting an inner edge of 50 au, position angle of $60 \pm 10°$, and inclination of $40 \pm 10°$ from face-on.

The orbital properties of HD 206893 B were revisited by Grandjean et al. (2019), who performed a joint fit to radial velocity (RV) monitoring, *Hipparcos* and *Gaia* astrometry, and SPHERE and NaCo imaging to infer an orbital period for the companion of 21–33 yr. They derived its dynamical mass to be a potentially planetary mass of $10^{+5}_{-4}M_{\text{Jup}}$. However, Grandjean et al. (2019) note that the fit appears dominated by the *Hipparcos-Gaia* proper motion constraints, as the estimated mass from the joint fit is inconsistent at the 2σ level with the mass derived from the combination of only direct imaging astrometry and RV variation. The authors thus posit that the 'B' companion cannot be responsible for the observed 1.6 year RV drift, and that this variation may correspond instead to an additional $\sim 15M_{\text{Jup}}$ interior companion with a short 1.6–4 year period.

In this study, we present Gemini Planet Imager (GPI; Macintosh et al. 2008) observations of the HD 206893 system at J, H, $K1$, and $K2$ bands with the goal of characterizing the imaged companion and providing the most comprehensive and highest-resolution spectral coverage to date. In Sections 2 and 3, we detail the GPI observations, data reduction, post-processing, and analysis techniques. Assessment of the host star properties are described in Section 4. Results are described in Section 5, including companion photometry, location in the color-magnitude diagram, atmospheric characterization, astrometric analysis, and limits on additional companions. We examine potential explanations for the reddening of the system in Section 6, and conclude by comparing HD 206893 B with the known population of directly-imaged companions and disk systems in Section 7.

2. OBSERVATIONS

The Gemini Planet Imager Exoplanet Survey (GPIES; Macintosh et al. 2014) is a dedicated 900-hour direct imaging survey to discover and characterize giant planets within a sample of over 600 nearby young stars using the GPI integral field spectrograph (IFS) at Gemini South observatory. As part of the GPIES campaign, IFS coronagraphic observations of HD 206893 were first obtained in H-band spectroscopic mode on UT 2016-09-22 (program ID GS-2015B-Q-01). The target was included in the campaign sample owing

Night (UT)	Band	$\lambda/\Delta\lambda$	Int. Time (min)	Field Rot. (°)	Airmass Range	Seeing (arcsec)
2016-09-22	H	44-49	37.7	32.7	1.05-1.06	0.68
2016-10-21	$K1$	62-70	73.5	59.7	1.05-1.09	1.17
2016-11-17*	$K2$	75-83	75.5	14.9	1.12-1.54	1.46
2016-11-18*	$K2$	75-83	71.5	14.6	1.12-1.40	1.44
2017-11-09	$K2$	75-83	88	24.1	1.08-1.32	†
2018-09-24	J	35-39	89	68.1	1.05-1.11	†

Table 1: Observation Summary. Datasets denoted with * are shown for reference but not used in the modeling analyses presented in this work due to lower SNR. The † denotes that facility seeing data were unavailable during the observations.

to its proximity, youth, and strong infrared excess, and the companion was noted in the preliminary data reductions. A total of 38×60-second IFS datacubes were taken under atmospheric conditions with $\sim 0\rlap{.}''68$ average seeing, close to the median DIMM seeing for Gemini South ($\sim 0\rlap{.}''65$). Observations were taken near target transit at a nearly constant airmass, achieving a total of $32.7°$ of field rotation and enabling Angular Differential Imaging (ADI; Marois et al. 2006a). To obtain wavelength calibration and account for instrumental flexure, argon arc lamp frames were taken immediately preceding the science observations. Additional H-band observations were taken in polarization mode following the spectroscopic imaging sequence, but are not included in this analysis.

Follow-up spectroscopy was obtained on UT 2016-10-21 in $K1$ (74×60-second frames; $59.7°$ rotation) and on UT 2016-11-17/18 in $K2$ (for a two-night total of 148×60-second frames; $29.5°$ rotation). Seeing conditions were worse than median in all three follow-up datasets, as shown in Table 1. The object was re-observed in $K2$ on UT 2017-11-09 with the same observing methodology, achieving additional field rotation under improved atmospheric conditions with lower residual wavefront error. The object was observed once more to obtain a J band spectrum on UT 2018-09-24. A summary of the instrument modes, observations, and seeing data is provided in Table 1.

3. DATA REDUCTION AND ANALYSIS

3.1. *GPI Data Reduction*

Calibrated spectral datacubes (x, y, λ) for datasets in each of the four bands were obtained from the raw IFS data using the GPI Data Reduction Pipeline v.1.4.0 (DRP; Perrin et al. 2016). Within the GPI DRP, raw IFS frames are dark subtracted then interpolated over bad pixels. The effects of instrumental flexure on the positioning of individual microspectra in the IFS frames are accounted for by aligning the contemporaneous arc lamp frames against a library of deep reference argon arcs (Wolff et al. 2014), producing a

wavelength calibration used to assemble spectral datacubes from the extracted microspectra (Maire et al. 2014). The resulting datacubes are then flatfielded, interpolated to a common wavelength axis, and corrected for geometric distortion (Konopacky et al. 2014), resulting in spectral datacubes with 37 channels each. The astrometric solution for GPI has been shown to remain constant within uncertainties (Konopacky et al. 2014; De Rosa et al. 2015), and we adopt plate scale and position angle values of 14.166 ± 0.007 mas/pixel and $-0.10 \pm 0.13°$E of N.

To align and register the images, the stellar position behind the GPI coronagraphic occulting mask was estimated using the four satellite spots present in each slice of the datacube (Wang et al. 2014). These spots are attenuated replica images of the stellar point spread function (PSF) introduced by the placement of a two-dimensional amplitude grating at the pupil plane (Marois et al. 2006b; Sivaramakrishnan & Oppenheimer 2006), and enable estimation of the object flux to stellar flux ratio (Wang et al. 2014). The adopted spot-to-star flux ratios for each filter and associated apodizer were 1.798×10^{-4} for J, 2.035×10^{-4} for H, 2.695×10^{-4} for $K1$, and 1.905×10^{-4} for $K2$ (Maire et al. 2014).

Outside of the GPI DRP, the fully-calibrated datacubes were further post-processed to subtract the contribution of the PSF and speckle noise. This was accomplished using three post-processing techniques: Locally-Optimized Combination of Images (LOCI; Lafrenière et al. 2007) for the J, H, and $K2$-band data, classical ADI (cADI; Marois et al. 2006a) for the $K1$ data, and pyKLIP for all four bands (Wang et al. 2015). In this work, the pyKLIP reductions from the auto-reduced GPI pipeline (Wang et al. 2018) are used to measure the achieved contrast and sensitivity to companions (see Section 5.5 and the reduced pyKLIP images in Appendix A), and the LOCI/cADI reductions are used for the companion spectral extraction and astrometry.

An apodized high pass filter following a Hanning profile (cutoff of 4 equivalent pixels) was applied to each frame to suppress slowly varying spatial frequencies within the data that are not well captured by PSF subtraction algorithms. The small amount of field rotation at H and increased speckle noise at J and $K2$ prevent a clean extraction of the companion with cADI, so LOCI was used to further process these bands. In order to reproduce images optimized to match the spatial distribution of speckles, the best-matched PSFs for each band were then estimated from a library of reference images with the following routine parameters: a PSF subtraction annulus of $d_r = 5$ pixels, optimized region for PSF comparison of $300\times$ the full-width at half-maximum (FWHM), geometry factor of $g = 1$, and separation criteria between regions of $N_\delta = 0.75$. For $K2$, the decreasing SNR of satellite spots near the red edge of the band, as well as the increased brightness of the companion, impacted the fidelity of

the spectral extraction, requiring a modified high-pass filter with a cutoff of 10 pixels. (Extractions of the $K2$ spectrum using various algorithms and filter sizes are presented in Appendix A.) The $K1$ data benefit from a large field rotation, and simple cADI was used to perform speckle subtraction, subtracting the stellar halo contribution by taking the median of all science frames and subtracting the median from each individual frame.

3.2. *Astrometry, Spectroscopy, and Covariance*

The astrometry of the companion was measured using the collapsed broadband PSF-subtracted datacubes. To extract spectroscopy of the companion, the process of injecting a negative fake planet was applied (cf. Marois et al. 2010). A negative template PSF with the estimated position and flux of the companion was inserted into the raw dataset, and then the post-processing pipelines applied above were repeated iteratively to minimize the residuals within a 2×2 FWHM region centered at the companion position, adjusting the x- and y-positions and flux of the companion in each iteration. This allowed for correction of any differences in algorithm throughput between the LOCI and cADI reductions. To correct for flux offsets between the $K1$ and $K2$ datasets in the overlap region of the two bands (from $2.10\,\mu$m – $2.20\,\mu$m), the $K1$ spectrum flux scaling was shifted to minimize the χ^2 value between the two spectra, resulting in a 4% downward shift.

As the raw IFS data include over 36,000 microspectra, the process of spectral extraction and interpolation (from the 16 pixel microspectra to 37 wavelength elements) introduces correlations between the resulting 37 spectral channels in the final datacubes. Applying the methodology of Greco & Brandt (2016), we calculate the covariance between channels to better estimate spectral uncertainties (see Appendix A), an approach that has been applied to other recent analyses of GPI companion spectra (cf., De Rosa et al. 2016; Johnson-Groh et al. 2017; Rajan et al. 2017). This effect can then be incorporated into the error budget of the individual spectrophotometric points for model fitting, as described in Section 5.3.

4. HOST STAR PROPERTIES

We derive stellar properties from comparison of the stellar SED to BT-NextGen stellar model atmospheres (Allard et al. 2012) combined with the MIST stellar isochrones (Dotter 2016; Choi et al. 2016). For each stellar model grid at a given mass and age, stellar radius, temperature, and surface gravity are estimated and synthetic photometry is derived. Figure 1 shows the combined Stromgren, Geneva, Tycho, *Hipparcos*, 2MASS and *WISE* photometry for HD 206893 A with the best-fit stellar atmospheric model overplotted. A Markov Chain Monte Carlo (MCMC) approach was applied

to determine the best-fitting model, with stellar age, mass, extinction, and distance as free parameters (following Nielsen et al. 2017; De Rosa et al. 2016). Uniform priors in age, mass, and A_v were applied, as well as a Gaussian distance prior centered at the observed *Gaia* parallax. The metallicity is assumed to be solar, concordant with the findings of Delorme et al. (2017). Figure 2 shows the posterior distribution of stellar properties from the MCMC analysis. Based upon the age posterior from these SED fits, we find that the stellar age is 601^{+420}_{-380} Myr with 1σ confidence. The best-fit stellar parameters are provided in Table 2. The large uncertainty on the stellar age from this approach is commensurate with the difficulty in determining precise age estimates for F5V stars, as noted in the detailed analysis of HD 206893 A by Delorme et al. (2017).
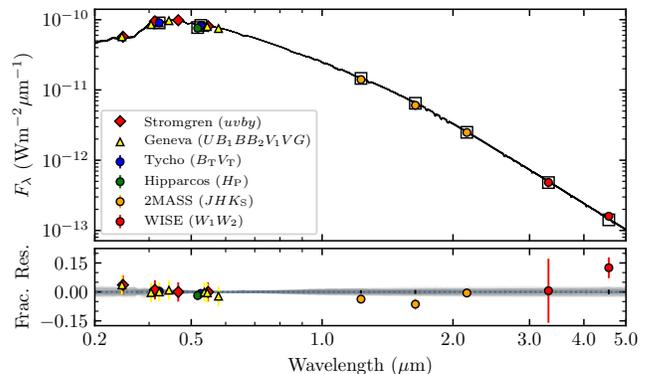

Figure 1: Stellar SED and best fit BT NextGen model spectrum for the primary star HD 206893 A, with residuals shown in the bottom panel. Best fit parameters correspond to intermediate age (601 Myr, albeit with large uncertainties of $^{+420}_{-380}$ Myr), and low extinction ($A_V = 0.07^{+0.05}_{-0.04}$).

HD 206893 A is not a known member of a stellar association, which would allow for a more precise age determination. We cross-checked the possibility of young moving group membership using the Bayesian Analysis for Nearby Young AssociatioNs (BANYAN) Σ tool (Gagné et al. 2018). Given *Gaia* DR2 values for stellar parallax, proper motion, and radial velocity[1] (Table 2; Gaia Collaboration et al. 2018), BANYAN Σ provides a 61.1% probability of membership in the Argus moving group, and a 38.9% probability of field membership.

The existence and age of the Argus association have been subject to debate, with estimates ranging from ∼40 Myr (Torres et al. 2008) to 268 Myr (Bell et al. 2015). The reality of the association has been called into question (Bell

---

[1] The RV drift of -0.1 ± 0.5 km/s identified in Grandjean et al. (2019) is within the *Gaia* DR2 uncertainty (-12.45 ± 0.59 km/s) and likely does not affect this kinematic estimate.
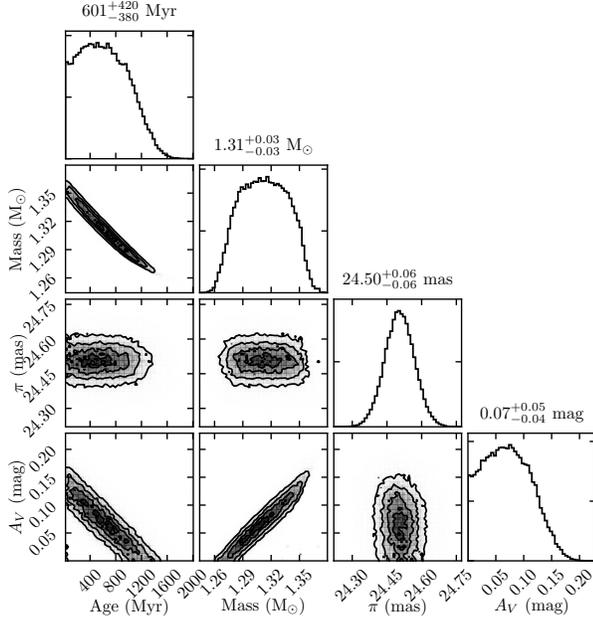
Figure 2: Posterior distribution of stellar properties of the primary star HD 206893 A. The asymmetric distribution on the stellar age suggests a broad range of ∼200 Myr to ∼1 Gyr at 1σ confidence.

et al. 2015), however, it has recently been re-established as a field association of age 40–50 Myr by Zuckerman (2019). From the low BANYAN Σ probabilities of both Argus and field membership ($< 80 - 90\%$), no definitive conclusion can be drawn. However, due to the unique kinematics of Argus and signatures of youth among its member stars, the association is also included in a recent Bayesian analysis of nearby young moving groups by Lee & Song (2019). Calculating the membership probabilities using the models of Lee & Song (2019) yields similar results to BANYAN Σ, with p(Argus) = 63%, p(Field) = 37%; kinematic comparisons are shown in Figure 3. Given the slight preference for Argus membership from both moving group assessments, we consider a range of possible ages in estimating companion properties. Specifically, we use the Baraffe et al. (2002) DUSTY and Baraffe et al. (2003) COND models at 50, 100, 120, and 500 Myr to estimate companion mass in Section 5.1, where the upper limit on age is set by the stellar SED analysis. At the same time, we note that the significant MIR and FIR excess of the system (Chen et al. 2014) also likely points to a younger age.
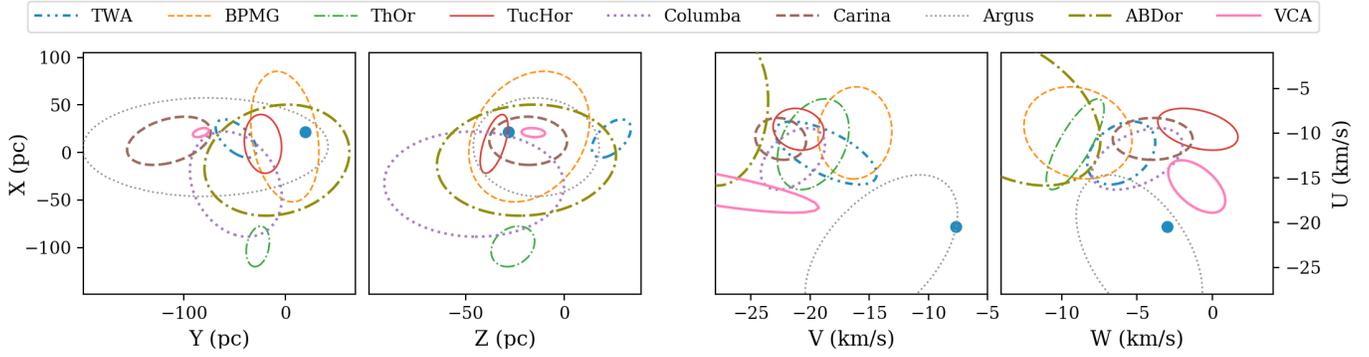
Figure 3: XYZUVW position of HD 206893 (blue point) compared to moving group models from Lee & Song (2019).
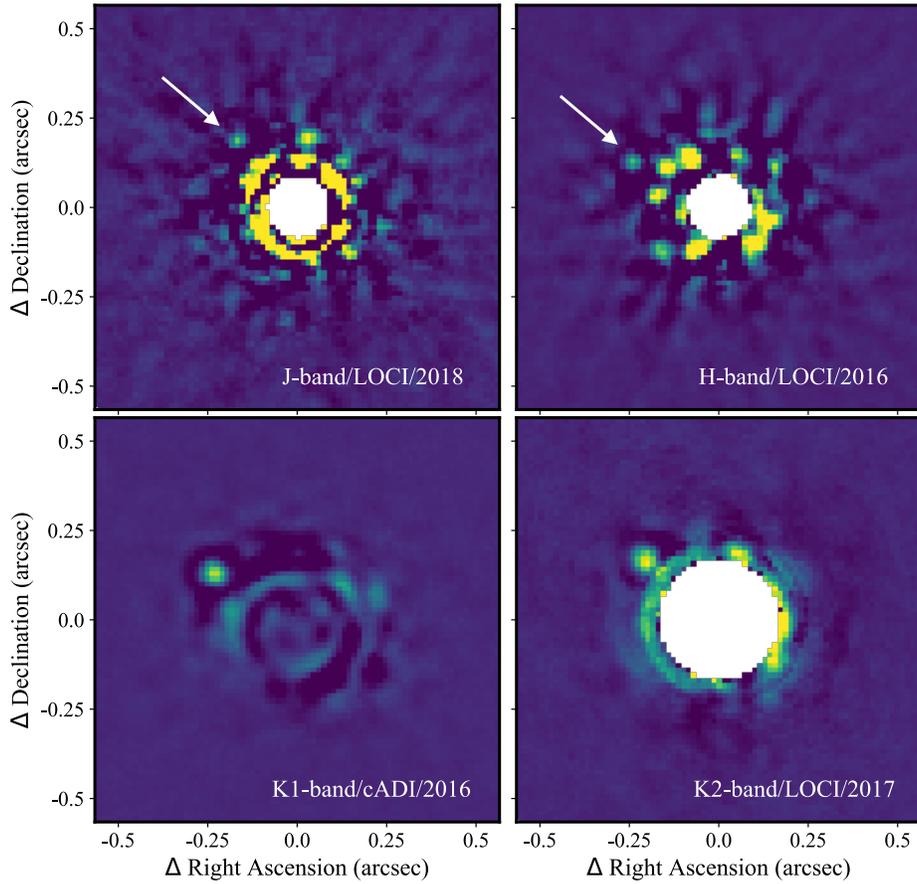

Figure 4: GPI PSF-subtracted images of HD 206893 B in J-band (upper left), H-band (upper right), $K1$-band (lower left), and $K2$-band (lower right), from the LOCI and cADI reductions. Each individual image is median-collapsed and scaled separately to minimize the contributions of residual speckle noise. Noticeable change in the companion position angle can be seen between the earliest 2016 epoch (upper right) and the latest 2018 epoch (upper left).

5. RESULTS

5.1. *GPI Images and Integrated Photometry*

Figure 4 shows the final median-collapsed GPI images in J, H, $K1$ and $K2$ bands from the LOCI and cADI reductions. The images show significant orbital motion of the companion between the earliest 2016 H epoch and the latest 2018 J epoch, as well as the higher SNR detections at redder wavelengths, consistent with the upward slope of the observed spectrum.

Broadband photometry for HD 206893 B was estimated from the GPI spectral datacubes by interpolating both 2MASS and Mauna Kea Observatory (MKO) transmission filter profiles (Tokunaga et al. 2002) to the GPI wavelength scaling. The J, H, and Ks (or K) filter profiles were convolved with a Gaussian filter of FWHM corresponding to each GPI band, then interpolated to the corresponding GPI wavelength grid. The GPI spectra (combining both $K1$ and $K2$ as described in Section 3.2 to cover the full K band) were then integrated over the J, H, and Ks or K bandpasses to derive the magnitudes in Table 2, accounting for zero point corrections. The derived photometry allows for positioning HD 206893 B on NIR color-magnitude diagrams (CMDs) of substellar objects, as shown in Figure 5. The derived photometry from GPI is consistent within uncertainties with the VLT/SPHERE magnitudes reported in Milli et al. (2017) and Delorme et al. (2017). The position of HD 206893 B on the NIR CMDs demonstrates its extraordinary red color, distinct among even the reddest planetary-mass companions, free-floating objects, and low-gravity and/or otherwise peculiar field objects.

System Property	Value		Unit	Ref.
Parallax	$26.08 \pm 0.53, 24.51 \pm 0.06$		mas	1, 2
Distance	$38.3 \pm 0.8, 40.8 \pm 0.1$		pc	1, 2
μ_α	$93.67 \pm 0.66, 93.78 \pm 0.09$		mas/yr	1, 2
μ_δ	$0.33 \pm 0.37, 0.02 \pm 0.08$		mas/yr	1, 2
Radial Velocity	-12.45 ± 0.59		km/s	2
Age	~ 50 (kinematics); 601^{+420}_{-380} (stellar SED)		Myr	1, 3, 4
A_V	$0.07^{+0.05}_{-0.04}$		mag	4
	HD 206893	HD 206893 B		
Spectral Type	F5V	$L4 - L8^{\dagger}$	-	1 / 4
M_J	2.82 ± 0.06	15.39 ± 0.04	mag	4
M_H	2.64 ± 0.06	13.68 ± 0.04	mag	4
M_{Ks}	2.54 ± 0.06	12.00 ± 0.07	mag	4
$M_{L'}$	2.48	10.39 ± 0.22	mag	1 / 4
J	5.87 ± 0.02	18.44 ± 0.03	mag	4
H	5.69 ± 0.03	16.73 ± 0.03	mag	4
Ks	5.59 ± 0.02	15.05 ± 0.07	mag	4
J_{MKO}		18.38 ± 0.03	mag	4
H_{MKO}		16.82 ± 0.03	mag	4
K_{MKO}		15.02 ± 0.07	mag	4
L'	5.52	$13.43^{+0.17}_{-0.15}$	mag	1 / 3
Mass	1.31 ± 0.03	12 / 20 / 20 / 40	$M_\odot, M_{\mathrm{Jup}}$	4
T_{eff}	$6500 \pm 100^*$	1200–$1800^{\dagger}$	K	3,4
$\log(g)$	$4.45 \pm 0.15^*$	3.0–$5.0^{\dagger}$	$\log_{10}(\mathrm{cm/s}^2)$	3,4

Table 2: Properties of the HD 206893 system. Photometry is provided in the 2MASS system, with MKO also provided for the companion. Companion photometry has been synthesized by integrating the GPI spectra over the relevant bandpasses accounting for differences in the 2MASS and MKO transmission profiles, as described in Section 5.1. Estimated masses for the companion in M_{Jup} are provided assuming a range of ages at 50, 100, 120, and 500 Myr. *Stellar parameters derived from FEROS spectroscopy by Delorme et al. (2017). †The large reported ranges in spectral type, effective temperature, and surface gravity reflect the difficulty in matching the observed companion spectrum to L-dwarf standard templates and atmospheric models; see Sections 5.2 and 5.3. **References.** (1) Milli et al. (2017), (2) *Gaia* DR2, Gaia Collaboration et al. (2018), (3) Delorme et al. (2017), (4) This work.
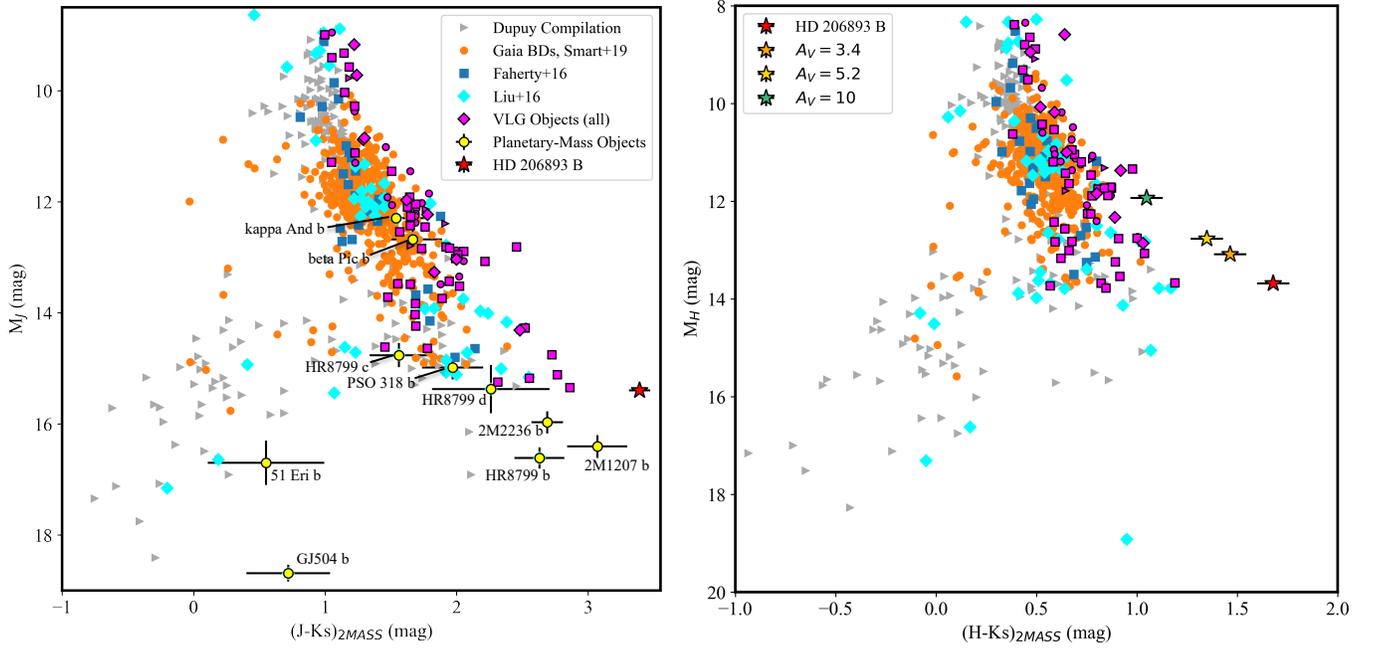
Figure 5: NIR color-magnitude diagrams of L- and T-type brown dwarfs and known planetary-mass objects in the 2MASS photometric system. Data are compiled from the following resources: field brown dwarfs with *Gaia* parallaxes from Smart et al. (2019) (orange circles); the Database of Ultracool Parallaxes (gray triangles; http://www.as.utexas.edu/~tdupuy/plx/Database_ of_Ultracool_Parallaxes.html) maintained by T. Dupuy, originally in Dupuy & Liu (2012), Dupuy & Kraus (2013), and Liu et al. (2016) (shown separately in cyan diamonds); and substellar objects considered analogous to planets (blue squares) from Faherty et al. (2016). Objects with low-gravity indicators are shown in magenta, demonstrating the known red offset of these objects from the field sequence. The left panel shows the M_J vs. $J - Ks$ CMD, with HD 206893 B indicated by a red star and benchmark planetary mass objects labeled (yellow circles). The right panel shows the M_H vs. $H - Ks$ CMD. At $H - Ks = 1.68$, HD 206893 B occupies a far redder space in the CMD than any other known substellar object. The additional points for HD 206893 B correspond to A_V values of 10 to 3.4 (left to right), adopted to match a similar range of extinction values estimated for the dusty, younger CT Cha system, and $A_V = 10$ shown in the green star to indicate the extreme values needed to reconcile the object position with the red edge of the substellar sequence.

5.2. *Composite Spectrum and Spectral Classification*

The resulting combined spectrum is shown in Figure 6 with each of the extractions from the reduced, post-processed J, H, $K1$, and $K2$ GPI datacubes. The VLT spectra and photometry from Milli et al. (2017) and Delorme et al. (2017) are also shown, demonstrating good agreement between GPI and SPHERE. The GPI $K2$ spectral slope beyond $2.2\,\mu$m was noted to be unusually steep in the first epoch of observations, and motivated a deeper second-epoch set of observations. The spectral morphology persisted between the two epochs of $K2$ data taken two years apart, and the steepness appears to be dependent upon the spectral extraction as described in Appendix A. For the remaining analysis in this work, only the extraction from the higher SNR $K2$ spectrum is used.

To determine the spectral properties of HD 206893 B in comparison with known brown dwarfs and atmospheric models, the combined spectra from SPHERE and GPI spanning Y to $K2$ were analyzed using the SpeX Prism Library Analysis Toolkit (SPLAT; Burgasser & the SPLAT Development Team 2017). Spectral typing was performed within SPLAT with a χ^2 minimization approach, classifying the object by template across the full ensemble of L0–T5 spectra in the SpeX Prism Library. Based on the exceptional redness of the spectrum, the resulting matches within the spectral library correspond to those of the coolest L-type objects, at L6±1 subclasses. While no single spectrum provides a close morphological match across the full Y–$K2$ range, the three closest matches within the spectral library were late-type, low-gravity objects, all with reduced χ^2 values of ~9: WISE J174102.78-464225.5 (>L5γ; Faherty et al. 2016), 2MASS J11193254-1137466 (L7γ, likely TW Hya member; Kellogg et al. 2015), and 2MASS J11472421-2040204 (L7γ, likely TW Hya member; Kellogg et al. 2016). When the SPLAT library comparison is extended to earlier spectral types, the closest matching objects correspond to M9 pre-main sequence stars with extreme levels of extinction (e.g., 2MASS J03444520+3201197 in IC 348 and 2MASS J04325026+2422115 in Taurus, with reduced χ^2 values of 7–8); given the distance and low extinction to HD 206893 and its companion absolute magnitude, these matches are not likely to share similar physical properties to HD 206893 B, and goodness-of-fit is driven by the redness of the object alone.

The large observed spread in NIR colors observed among L-dwarfs of the same optical spectral type (e.g., Leggett et al. 2003; Faherty et al. 2013) has motivated efforts to produce a systematic means of spectral typing, including qualitative comparison on a band-by-band basis to account for variations in NIR spectral morphology for objects of the same optical spectral classification. Following the work of Cruz et al. (2018), which aims to reconcile differences in NIR spectral features for the L-dwarf population, we compare the HD 206893 B spectrum to an ensemble of L-dwarf field and low-gravity standards using the Ultracool Typing Kit (UTK[2]; Abrahams & Cruz 2017). The UTK analysis is shown in Figure 7, and involves normalizing each J, H, or K spectrum individually and comparing the normalized spectra with the spectral templates. The comparison demonstrates the dissimmilarities between HD 206893 B and typical L-dwarfs. The spectra are qualitatively similar to the later field and young L populations, commensurate with the SPLAT typing analysis. However, the steep slope of the blue side of H-band and peaked morphology more closely match the low-gravity population than field objects, potentially indicating youth (although challenges exist in using the triangular shape to reliably distinguish dusty atmospheres from low-gravity ones; Allers & Liu 2013). Figure 8 shows the three closest spectral matches from SPLAT, including 10 Myr old candidate TW Hya members, in addition to the unusually red AB Doradus member WISEP J004701.06+680352.1 (Gizis et al. 2012). Spectra have been normalized per band over the same normalization ranges used in UTK, extending a similar analysis to later low-gravity L-dwarfs. These late-type comparisons show the greatest morphological similarities to HD 206893 B, particularly across J and H band when normalized on a band-by-band basis. As such, we adopt a conservative range of L6±2 for the companion spectral type, noting stronger similarities to young low-gravity objects in this spectral range than to the late-type field population seen in Figure 7.
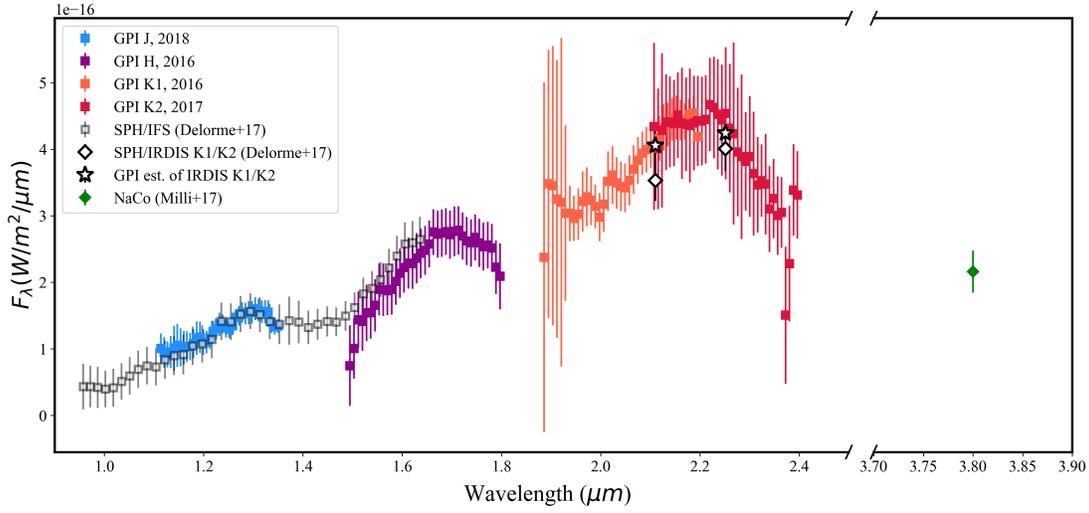

Figure 6: Combined GPI J, H, $K1$, and $K2$ spectra of HD 206893 B, overlaid with the spectra and photometry from Milli et al. (2017) and Delorme et al. (2017), which show good agreement between the SPHERE IFS and GPI spectroscopy. IRDIS $K1/K2$ photometry has been synthesized from the GPI spectra (white stars) to enable a comparison with the measured SPHERE photometry (white diamonds).
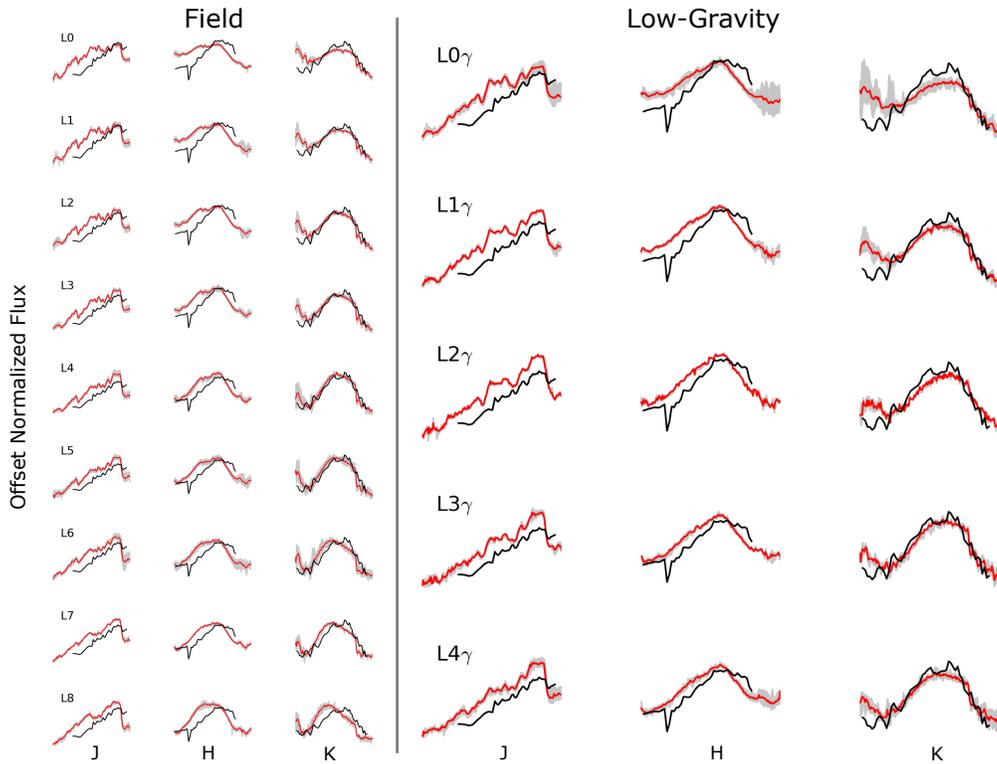

Figure 7: Comparison of the combined GPI+SPHERE spectra (black) to a suite of L-dwarf standard templates of varying gravity (red) using the Ultracool Typing Kit (Abrahams & Cruz 2017). The low-gravity (γ) standards from Cruz et al. (2018) include only spectral types up to L4. Each band is independently normalized using the band-specific normalization ranges described in Cruz et al. (2018): 0.87-1.39μm for *zJ*, 1.41-1.89μm for *H*, and 1.91-2.39μm for *K*. Morphologically, the HD 206893 B spectrum appears most similar to late, low-gravity objects.
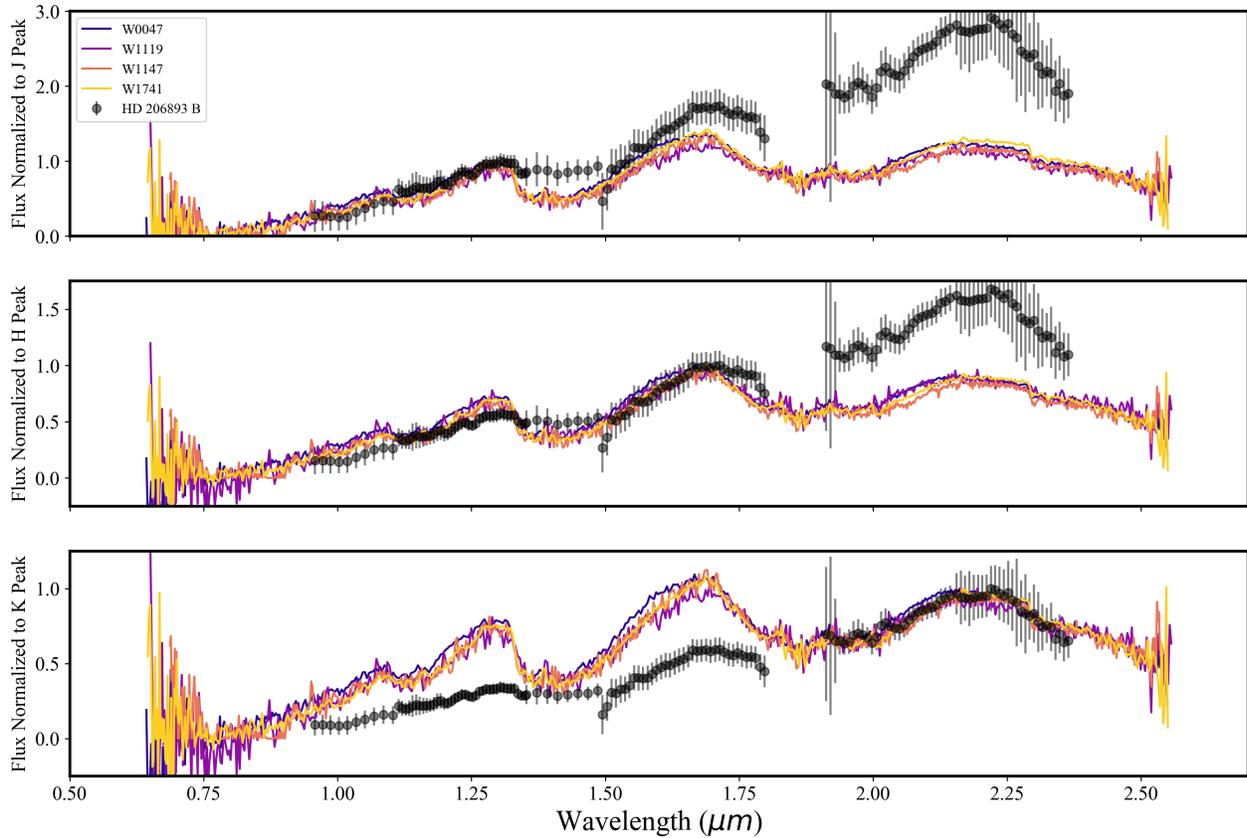
Figure 8: Comparison of the combined GPI+SPHERE spectra (black) to young, low-gravity L5–L7 objects, including the closest substellar spectral matches in the SpeX prism library. Each panel has been normalized on a band-by-band basis to the peak of J, H, or K (top to bottom). Normalization at shorter wavelengths shows good morphological matches to each of J and H and emphasizes the shallowness of the water band at $1.4\,\mu$m.

Model Grid	$T_{\rm eff}$ (K)	log[g (cgs)]	Notes
Sonora	1100-1600	3.75-5.0	Solar metallicity, $f_{\rm sed}$ = 1
Cloudy-AE 60	600-1700	3.5-5.0	Solar metallicity, fixed 60 μm particles
DRIFT-PHOENIX	1000-2000	3.0-5.0	Solar metallicity, super-solar [M/H] = 0.3
BT-Settl	1200-2050	2.5-5.5	Solar metallicity

Table 3: Parameter ranges in the model grid search. For all models tested, the object radius was scaled by factors ranging from 0.5 - 3.5 $R_{\rm Jup}$ in the model fitting, in steps of 0.01.

5.3. *Brown Dwarf Atmospheric Modeling*

The combined spectra and photometry of HD 206893 B from GPI, SPHERE, and NaCo, spanning 0.95 to 3.8μm, were compared to four grids of theoretical atmosphere models in order to derive estimates of effective temperature, surface gravity, and metallicity. The model grids used were: **(1)** a subset of the Sonora models, a new model grid designed for substellar and young giant planet atmospheres (Marley et al. 2020, in prep.; see also the currently available solar metallicity cloud-free grid from Marley et al. 2018)[3], **(2)** the Cloudy-AE[4] models, originally developed for the HR 8799 planets (Madhusudhan et al. 2011), **(3)** the DRIFT-PHOENIX[5] Atmosphere Models (Helling et al. 2008; Witte et al. 2009, 2011), and **(4)** the BT-Settl (2015)[6] grid (Allard et al. 2012; Allard 2014). For each grid, individual models spanning ranges of $T_{\rm eff}$ and log(g) space were binned to the resolution of the GPI spectra and interpolated over the GPI wavelength axes. All models used were of solar metallicity, with the exception of DRIFT-PHOENIX, which included both solar and super-solar [M/H] values. Object radius was treated as a fit parameter, with each model scaled to match the object SED using the *Gaia* DR2 distance and a range of plausible object radii. The explored parameter ranges for the model grids are summarized in Table 3, scaling the object radius from 0.5–3.5 $R_{\rm Jup}$ in steps of 0.01. The resulting χ^2 fit statistics were calculated accounting for covariances in spectral channels, following the approach outlined in De Rosa et al. (2016), with zero-valued covariance assigned to the SPHERE IFS Y and J/H data not covered by GPI. Best fit models were determined separately for each band and for the full spectrum, allowing us to investigate disparities between best fit models between wavelength regimes. The resulting best fit models from the Sonora, DRIFT-PHOENIX, Cloudy-AE, and BT-Settl grids are shown in Figure 9 and incorporate covariances. Results from a standard covariance-free χ^2 approach are also shown on a band-by-band basis with faint dashed lines in Figure 9, the results of which are summarized

[3] http://doi.org/10.5281/zenodo.1309035

[4] https://www.astro.princeton.edu/~burrows/8799/8799.html

[5] http://svo2.cab.inta-csic.es/theory/newov

[6] https://phoenix.ens-lyon.fr/Grids/BT-Settl/CIFIST20112015

in Appendix B. While the standard fits without covariance estimation sometimes more closely visually match the GPI spectral data points, the derived physical parameters are in better agreement across bands when accounting for spectral covariance.

Given the extraordinary redness of the companion, none of the models provides a qualitatively good fit to the full spectrum, and reduced χ^2 statistic values range from ∼1.2 to 8. The best fits to the Sonora and Cloudy-AE60 models all lie at the edge of the available grid parameters (Table 3), suggesting that the best-fits likely reside outside of the range of the current model grids. As noted in Delorme et al. (2017), the unusual SED of the object and its extreme spectral features present significant discrepancies relative to existing model atmosphere grids, necessitating additional sources of reddening. Challenges in atmospheric model fitting of L-dwarfs, particularly in the reproduction of the NIR spectral slope and H-band morphology of young/low-gravity objects, have been noted in previous studies (e.g., Manjavacas et al. 2014) and have been attributed to the treatment of dust in current theoretical atmosphere models. We explore this possibility further in Section 6.2, and note that determining the cause of mismatches between observations and current models may involve considering a wide range of particle properties, overall dust content, and multispecies gas opacities, tasks well-suited for retrieval-based methods.

When we fit the full spectrum, the best-fit results from each model grid show a range of physical parameters; temperatures range from 1200 to 1700 K, surface gravities from log(g) of 3.5 to 5.0, and object radii from 0.96 to 1.55 $R_{\rm Jup}$. However, the derived properties vary significantly when comparing results across fits to individual bands. The derived log(g) values from the model fits and the inferred radii necessary to scale the flux are inconsistent, a discrepancy noted for previous fits of exoplanet spectra and photometry (e.g., HR8799bcd, beta Pic b, 51 Eri b, and others; Marois et al. 2008; Marley et al. 2012; Morzinski et al. 2015; Rajan et al. 2017). A detailed assessment of the full-spectrum fitting using each model grid, as well as brief summaries of model grid properties, are provided in Appendix B.

Following the methodology applied for spectral typing the object, we performed fits to the four GPI bands individually for each set of model grids, in addition to the full spectral fit. These fits are shown in the four subpanel rows of Figure 9, and each fit accounts for spectral covariance within that band. Accounting for spectral covariance, the best fit models agree within 100 K across all four bands for the Sonora and CloudyAE-60 models and across $JHK2$ for DRIFT-PHOENIX and BT-Settl. Departures in $K1$ for the DRIFT-PHOENIX and BT-Settl model grids may be attributed to the higher level of spectral covariance in the $K1$ band. Similarly, the high level of spectral correlation observed in H-
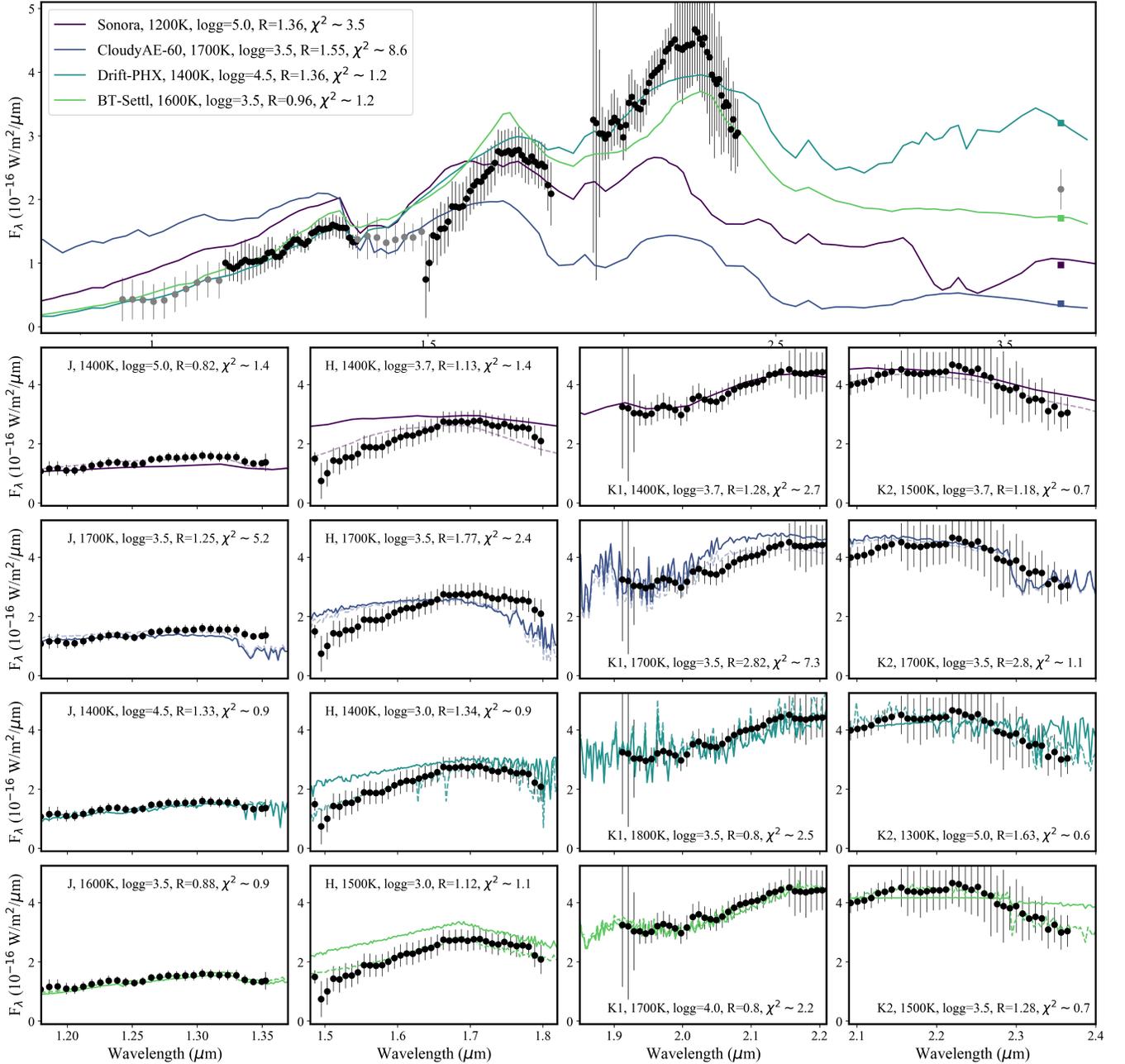
Figure 9: Best-fit models from a grid comparison of the GPI spectra (black points) and SPHERE+NaCo spectra and photometry (gray points) with four theoretical atmosphere models (Sonora in purple–Marley et al. 2020 in prep.; Cloudy-AE60 in blue –Madhusudhan et al. (2011); DRIFT-PHOENIX in dark green–Helling et al. (2008); Witte et al. (2009, 2011); and BT-Settl in light green–Allard et al. (2012)). The topmost panel shows the best-fits to the full spectral coverage from the combined SPHERE, GPI, and NaCo data. The integrated L' flux is shown for each set of models in square symbols. The four rows of subpanels show the results from fitting the four GPI bands separately. Corresponding χ^2 best-fit model parameters with (solid lines) and without (faint dashed lines) incorporation of covariances are shown in each panel.

band leads to a mismatch between the best fit models and datapoints for all four suites of models, an effect observed in previous IFS studies (e.g., Rajan et al. 2017). For comparison, the best fit models adopting a standard χ^2 approach are shown in light dashed lines within each panel. The estimated $\log(g)$ values are consistent across bands only for the Sonora and Cloudy-AE60 models, favoring lower-gravity fits. Each of the other three model suites provide a broad range of surface gravities and radii depending on the band in question.

5.4. *Astrometric Analysis*

The four new astrometric epochs from the GPI observations presented here were combined with five additional astrometric measurements from VLT/SPHERE and VLT/NaCo (Milli et al. 2017; Delorme et al. 2017; Grandjean et al. 2019) to explore the range of potential orbital parameters for HD 206893 B. The full set of astrometric measurements used in this analysis is provided in Table 4. Following the astrometric analyses described in De Rosa et al. (2015) and Rameau et al. (2016), a parallel-tempered Bayesian MCMC approach using the *emcee* package (Foreman-Mackey et al. 2013) was used to simultaneously fit eight companion orbital parameters, namely: semi-major axis (a), inclination (i), eccentricity (e), sums and differences of longitude of ascending node and argument of periastron ($\Omega \pm \omega$), epoch of periastron passage (τ), orbital period, and system parallax. We adopt the following standard prior distributions on the orbital parameters: log uniform in a, uniform in e and $\cos(i)$, and Gaussian for the system mass and system parallax. We initialized 512 walkers at 16 different temperatures; the lowest temperature samples the posterior distribution, while the highest temperature samples the prior. We advanced each chain for one million steps, saving every hundred steps. The first half of the chain was discarded as a "burn-in" period to ensure the final posterior distributions were not a function of the initial positions of the walkers.

Epoch	Separation (mas)	Pos. Angle (°)	Instrument, Band	
2015-10-05	270.4 ± 2.6	69.95 ± 0.55	SPH/IRDIS, H	1
2016-08-08	269.0 ± 10.4	61.6 ± 1.9	VLT/NaCo, L'	1
2016-09-16	265 ± 2	62.25 ± 0.11	SPH/IRDIS, $K1/K2$	2
2016-09-22	267.6 ± 2.9	62.72 ± 0.62	GPI, H	3
2016-10-21	265.0 ± 2.7	61.33 ± 0.64	GPI, $K1$	3
2017-07-14	260.3 ± 2	54.2 ± 0.4	SPH/IRDIS, H	4
2017-11-09	256.9 ± 1.1	51.01 ± 0.35	GPI, $K2$	3
2018-06-20	249.11 ± 1.6	45.5 ± 0.37	SPH/IRDIS, $H2/H3$	4
2018-09-24	251.7 ± 5.4	42.6 ± 1.6	GPI, J	3

Table 4: Astrometry for HD 206893 B. **References.** (1) Milli et al. (2017), (2) Delorme et al. (2017), (3) This work, (4) Grandjean et al. (2019).

The resulting posterior distributions for a subset of selected orbital parameters are shown in Figure 10. The 1σ

confidence intervals from the posterior distributions suggest a tightly constrained semi-major axis of $10.4^{+1.8}_{-1.7}$ au, orbital inclination of $145.6^{+13.8}_{-6.6}$ deg, and apoapsis distance of $11.7^{+2.7}_{-0.6}$ au, and place less restrictive constraints on the eccentricity ($0.23^{+0.13}_{-0.16}$) with a corresponding period range of $29.1^{+8.1}_{-6.7}$ years. The narrower posterior distribution on the apoapse distance is consistent with observing the companion near apastron, with the uncertainty on semimajor axis dominated by a less-stringent constraint on the radius of periapsis. This can also be seen in the covariance of semimajor axis and eccentricity posterior distributions in Figure 10, which favor smaller values of a for more eccentric ($e > 0.2$) orbits.

We investigated the co-planarity of the orbit of the companion with the spatially-resolved debris disk by comparing the inclination and position angle of the visual orbit on the sky to those estimated for the debris disk by Milli et al. (2017). The disk inclination and position angles are defined over more restrictive ranges than for a visual orbit; the disk is not measured to orbit in a particular direction around the star, and a 180 degree ambiguity exists in the position angle measurement. Under the assumption that the disk and orbital plane of the companion are non-orthogonal, we adopt an inclination for the disk of $i_d = 140° \pm 10°$, and a position angle of $\Omega_d = 60° \pm 10°$. We drew random variates from two Gaussian distributions describing these parameters for each sample of the posterior distribution of the visual orbit, assuming that the measured geometry of the disk and the fit to the visual orbit are uncorrelated. We measure the mutual inclination, i_m, between the disk and orbit using the following relation:

$$\cos(i_m) = \cos(i_c)\cos(i_d) + \sin(i_c)\sin(i_d)\cos(\Omega_c - \Omega_d) \tag{1}$$

where the c and d subscripts refer to the companion and disk, respectively. The resulting distribution of i_m and correlations with the other orbital elements are shown in Figure 10. The position angle of nodes for the orbit of the companion (Ω) is plotted from 0–180°, the same restricted range as the position angle of the disk. An equally good fit to the visual orbit can be found with $\omega + \pi$ and $\Omega + \pi$, however these orbits would be significantly misaligned with the assumed disk position angle of $60° \pm 10°$. The distribution of mutual inclinations for two randomly-oriented planes is also shown for reference, and i_m appears significantly shifted towards more co-planar solutions relative to this prior distribution. The current measurement precision for both the disk geometry and the visual orbit are not sufficient to exclude moderately misaligned configurations ($i_m \sim 20°$).

A representative sample of 250 orbits drawn randomly from the posterior distribution is shown in Figure 11. The plotted orbit colors indicate the mutual inclination value for the companion orbit relative to the disk geometry inferred
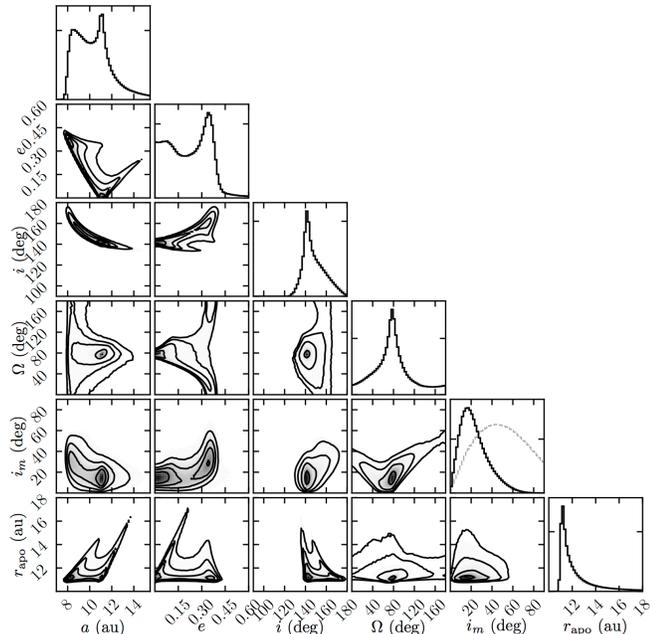
Figure 10: Posterior distributions for semimajor axis, eccentricity, inclination, longitude of the ascending node, mutual inclination of the companion orbit and circumstellar disk (with respect to the inferred disk geometry from Milli et al. 2017), and the radius of apoapsis. The gray dashed line overplotted represents the prior distribution in mutual inclination, showing that the posterior distribution slightly favors more co-planar over more misaligned configurations.

Figure 11: Subsample of 250 randomly-sampled MCMC orbits to HD 206893 B based on four epochs of GPI astrometric monitoring (blue diamonds) in addition to five epochs of VLT/SPHERE (black circles) and VLT/NaCo (red square) astrometry, covering a total time baseline from 2015-2018 (astrometric points and errors shown in inset). The darker orbits correspond to orbits with lower values of mutual inclinations between the companion orbit and the disk plane, with the mutual inclination distribution in Figure 10 peaking at $\sim 20°$.

from modeling in Milli et al. (2017), favoring more co-planar configurations. Misaligned configurations with greater values of i_m are generally more eccentric, corresponding to smaller semimajor axis and periapse distance, which can be seen from the posterior covariances in Figure 10. The long tail of the posterior distribution for apoapse distance, $r_{\rm apo}$, extends to large values coincident with the estimated inner edge of the disk at ~ 50 au by Milli et al. (2017).

5.5. *Sensitivity to Additional Companions*

From the pyKLIP reductions described in Section 3 and shown in Figure 18, we calculate contrast curves for each GPI band. These curves are shown in Figure 12; they are calculated by estimating noise levels from the PSF-subtracted images and correcting for instrument throughput, calculated by injecting and recovering false planets with L-type spectra (see Wang et al. 2018). The sensitivity to companions is then estimated from the contrast curves following the methodology of Nielsen et al. (2019). In brief, a synthetic population of 10^4 companions is drawn from a grid sampling mass and semi-major axis values, and each companion is randomly assigned orbital parameters (inclination, eccentricity, argument of periastron, and epoch of periastron passage). Projected
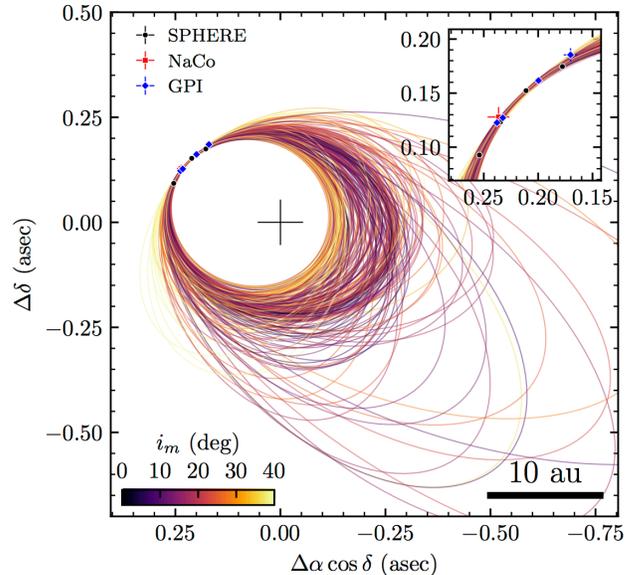
separation and magnitude difference are estimated and compared to the contrast curve to determine detection probability. Variation in contrast by epoch is accounted for by stepping the companion orbit forward in time in order to generate a new estimation for companion separation and contrast that can be compared to the observed contrast curve. The recovery rate for companions at a given mass and semimajor axis is then translated into a completeness percentage. The results are shown in Figure 13, where the mass of HD 206893 B corresponds to an assumed system age of 250 Myr. It is possible to exclude additional companions in the GPI images in the planetary regime down to 5 $M_{\rm Jup}$ at ~ 20 au, and in the brown dwarf regime down to ~ 10–20 $M_{\rm Jup}$ at ~ 10 au. For comparison, the inner additional companion signal predicted from RV variation by Grandjean et al. (2019) suggests a ~ 15 $M_{\rm Jup}$ object at an orbital separation of 1.4–2.6 au. The requisite contrast to detect such an object ($< 10^{-4}$ in the NIR at a separation of 50–60 mas) is beyond the sensitivity limits of current extreme AO direct imaging instruments and can be compared to the contrast curves and sensitivity of our data shown in Figures 12 and 13.
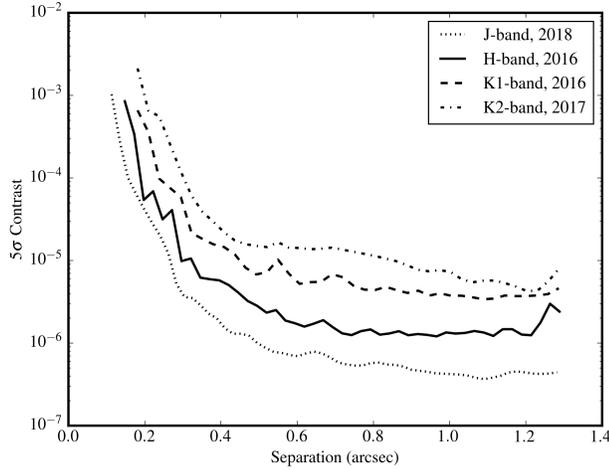
Figure 12: 5σ contrast curves calculated for the pyKLIP-reduced GPI images in each band of observation, assuming L-type object spectra.
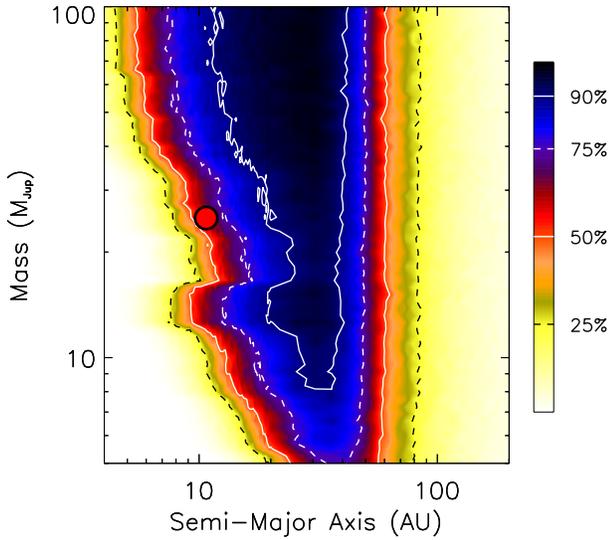

Figure 13: Combined sensitivity of all epochs and bands of GPI observations, expressed in terms of companion masses as a function of orbital separation. PyKLIP contrasts from Figure 12 are converted into physical parameters following the methodology of Nielsen et al. (2019) using an assumed age of 250 Myr and the CIFIST2011 BT-Settl atmosphere models (Caffau et al. 2011; Allard 2014; Baraffe et al. 2015) combined with the COND evolutionary sequences (Baraffe et al. 2003). The 'divot' seen at 10 au and ∼12 $M_{\rm Jup}$ corresponds to the closer inner working angles accessible in only the shorter wavelength observations. The colorbar and scale show corresponding completeness levels, with the approximate mass and semimajor axis of HD 206893 B for reference (red point).

6. DISCUSSION

6.1. *Companion redness and system extinction properties*

Given the existence of circumstellar material in the HD 206893 system, dust extinction may have an effect on the measured companion magnitudes; however, the nature of reddening in the system is currently unknown. The unusual redness of the companion could be explained by a range of reddening sources, namely: conventional interstellar reddening, extinction due to the debris disk, the presence of circumsecondary disk material around the companion itself, or dust within the atmosphere of the companion itself.

We adopted reddening values of $A_V = 3.4$ and 5.2, in conjunction with the extinction laws of Rieke & Lebofsky (1985), to estimate potential shift in color-magnitude space due to extinction caused by dust in the vicinity of the companion. These values for A_V were chosen from best-fit extinction estimates for the substellar companion in the CT Cha disk system (Schmidt et al. 2008; Wu et al. 2015). As CT Cha is considerably younger ($\sim$2 Myr) than HD 206893, this is likely an overestimate of potential extinction caused by the far less optically-thick HD 206893 debris disk. The resulting de-reddened CMD positions are shown in the right panel of Figure 5, with an additional value of $A_V = 10$ shown for comparison to illustrate the extreme and likely unphysical amount of extinction required to meet the red edge of the field L-dwarf sequence.

To determine which extinction estimates correspond to realistic values for a companion viewed edge-on within a debris disk, we compare dust column density and optical depth estimates to typical circumstellar disk values. Using standard relations for visual extinction and gas column density for the interstellar medium (N_H (cm^{-2}) $= 2.21 \times 10^{21} A_V$ (mag); Güver & Özel 2009), and translating this relation into a dust column density using the canonical 100:1 gas to dust ratio yields a dust mass column density of 3.7×10^{-4} g cm^{-2} for $A_V = 10$. For comparison, visual extinction for the edge-on AU Mic debris disk system with higher fractional infrared luminosity (3.9×10^{-4}; Matthews et al. 2015) has been estimated as $A_V = 0.5$ (Yee & Jensen 2010). Assuming small grains and a typical silicate density (0.5 μm and 3.27 g cm^{-3}) yields a particle column density of 2×10^8 grains/cm^2, suggesting that a debris disk with $A_V = 10$ is unrealistically optically thick ($\tau \sim 1.7$). We thus conclude that the companion's extreme redness is not likely to be caused by the debris disk, nor is this level of extreme optical depth likely in a circumsecondary disk. Further effects of reddening due to the disk environment are explored in detail in Section 6.3. The A_V estimate of 0.03 from stellar SED modeling in Figure 2 also argues against a significant reddening effect due to interstellar extinction, leaving dust in the companion atmosphere as the most viable scenario.

6.2. *Atmospheric reddening from dusty aerosols*

The known L-dwarf population exhibits a wide range of atmospheric color in the NIR, spanning $\sim$1.5 magnitudes in $J - K_s$ (Faherty et al. 2013). In particular, young L-dwarfs associated with moving groups have redder NIR colors than field counterparts of the same spectral type, an effect attributed to lower surface gravities that retain clouds at high altitude (Marley et al. 2012). From a large survey of 420 ultracool dwarfs, Kellogg et al. (2017) found similar ($\sim$2%) fractions of unusually red objects in both younger ($<$200 Myr) and older ($\geq$200 Myr) populations, an age delineation corresponding to the halting of gravitational contraction within ultracool evolutionary models (e.g., Burrows et al. 2001; Baraffe et al. 2015) and roughly correspondent to the demarcation between very-low to intermediate gravity indicators from Allers & Liu (2013). While age and peculiarity of ultracool objects are difficult to precisely quantify, a significant population of reportedly older red L-dwarfs exists (cf. Looper et al. 2008). Inclination angle has also been invoked as a potential explanation for discrepant red colors, as substellar objects viewed equator-on have redder infrared colors for the same spectral type than those viewed pole-on (Kirkpatrick et al. 2010; Vos et al. 2017).

Reasons for persistence of redder colors in moderate age, high-gravity objects remain uncertain. However, the presence of upper-atmosphere dusty aerosols of sub-micron sized grains has been put forth as a potential explanation. In this framework, small, cool dusty aerosols high in the atmosphere scatter (but do not emit) thermal flux. The sensitivity of scattering efficiency to wavelength for such particles is small compared to the wavelength of interest, thus producing a reddening. Marocco et al. (2014) and Hiranaka et al. (2016) examined such extinction effects in peculiar red L-dwarf atmospheres by assuming a population of sub-micron grains in the upper atmosphere. Marocco et al. (2014) adopted a dereddening approach with wavelength-dependent corrections based on standard interstellar extinction laws (Cardelli et al. 1989; Fitzpatrick 1999), and showed that applying dereddening using common dust compositions could make peculiar red objects appear similar to the field L-standard population. The HD 206893 B analysis by Delorme et al. (2017) identified the spectral type as L5–L7, concordant with its extremely red $Js - K1$ color, and they applied a similar method, generating extinction profiles with a range of A_v (up to A_v=10) and particle sizes (from 0.05 to 1 μm). However, corresponding objects in the same region of the NIR CMD exhibit significantly deeper water absorption features at 1.4 μm and much bluer slopes than those evident in the spectrophotometry of HD 206893 B, regardless of youth. By comparing the de-reddened spectrum of HD 206893 B to standard objects using a Cushing G analysis, Delorme et al. (2017) determined the closest matches to be those of field or

young L3.5 dwarfs, reproducing the slope of the SPHERE spectrophotometry.

In Hiranaka et al. (2016), extinction profiles generated from Mie scattering models with various grain sizes, size distributions, and compositions were fit to extinction profile estimates derived by dividing spectra of unusually red L-dwarfs by those of typical field L-dwarfs. In this work, we apply the same methodology and compare the full NIR spectrum of HD 206893 B to known L-dwarfs in order to investigate potential small dust grain populations that may be responsible for the observed reddening.

Figure 14 shows the full spectrum of HD 206893 B divided by L5, L6 and L7 spectral standards, selected as objects with median J-Ks colors for their spectral classes from the field gravity template sample in Cruz et al. (2018). Dividing the normalized spectrum of the standard by the normalized companion spectrum yields a visualization of the observed reddening, shown as the flux ratio of the two objects. The reddening profile is then fit by grain populations with various scattering properties, which may be used in turn to de-redden the companion spectrum. Initial treatments of dust in very low-mass stellar atmospheres recognized that the condensation temperatures of species such as enstatite ($MgSiO_3$), iron (Fe), forsterite (Mg_2SiO_4), and corundum (Al_2O_3) occurred in the photospheres of cool M-dwarfs (e.g., Tsuji et al. 1996) and many additional grain compositions with cool condensation temperatures have since been incorporated into atmospheric models treating dust (e.g., $\sim$30 various species of dust; Allard et al. 2001). As in Hiranaka et al. (2016), we use Mie scattering models and the refractive indices of various species to determine extinction coefficients. We adopt a standard power-law distribution $n(a) = a^{-3.5}$ with grain sizes from 0.1-1 μm and use the Mie scattering code LX-MIE (Kitzmann & Heng 2018) to calculate extinction curves for particles of forsterite, corundum, and TiO_2. As all three species produced similar extinction profiles and grain parameters, we focus here on the results from the forsterite grain fitting.

Given the previous Delorme et al. (2017) analysis demonstrating the closest spectral approximation of HD 206893 B to a reddened atmosphere of spectral type L3 (consistent with both field and younger AB Dor member L3 objects), we perform extinction fitting with an extinction curve derived from the flux ratio of HD 206893 B to a low-gravity L3γ object (2MASSW J2208136+292121; Kirkpatrick et al. 2000)[7], and

---

[7] We note that the L3γ object J2208 was identified as a β Pic candidate by Gagné et al. (2014), while an updated parallax and CMD analysis by Liu et al. (2016) show that it is marginally more similar to the field CMD sequence than that of very low gravity objects, making its youth determination slightly uncertain; however, the latter authors conclude that it remains a promising candidate member of the young moving group.
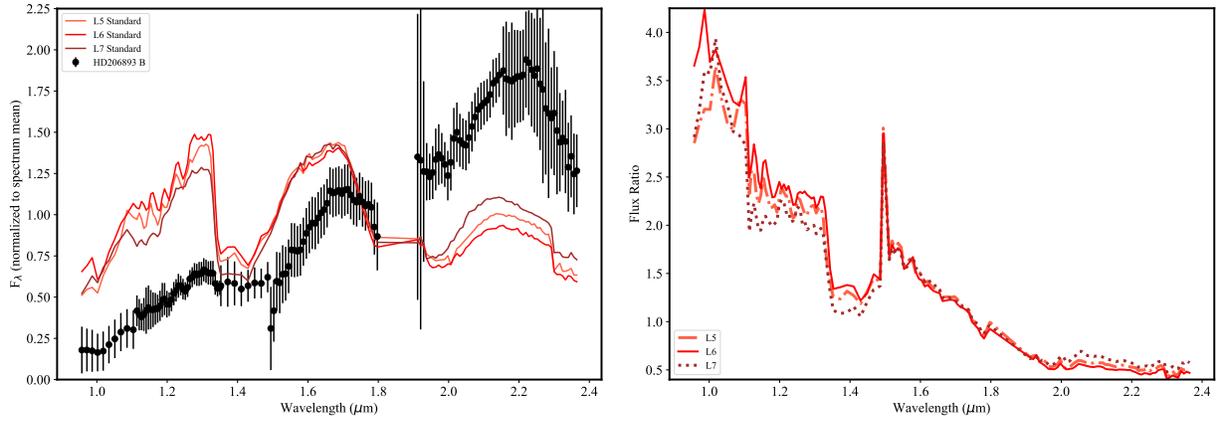
an unusually red field object with NIR spectral type L6.5pec (2MASSW J2244316+204343; Dahn et al. 2002; McLean et al. 2003; Looper et al. 2008). Fits to each of the extinction curves were performed using a Bayesian MCMC approach (the *emcee* package; Foreman-Mackey et al. 2013) to estimate particle column density, mean grain radius, and opacity scaling. The best fit curves from the MCMC analysis are shown in Figure 15. For the earlier very low gravity L3 spectral type, the corresponding posterior distributions are shown in Figure 16, with a best fit column density of 2.8×10^8 particles/cm^2, mean particle radius of 0.27 μm, and a constant vertical offset term of $C = -1.9$ which corresponds to a gray atmospheric opacity scaling term between the object and the field spectrum. For the peculiar L6.5, the best fit values have slightly lower column density (2.5×10^8 particles/cm^2), and smaller mean particle radius (0.20 μm), with a constant vertical offset term of $C = -0.43$.

In Figure 17, we show the result of applying the best-fit extinction curve for forsterite to effectively "de-redden" the full spectrum of HD 206893 B and compare it both the low gravity L3 object and unusually red field L6. The de-reddened spectra correspond closely to the L6.5 over J-band and similarly to both the L3 and L6.5 over H bands, albeit with a weaker water absorption feature at 1.4 μm, and more closely replicates the peaky H-band shape of the lower-gravity L3 than the broader morphology of the L6.5. The shallowness of the water band is consistent with the presence of significant dust in the object atmosphere; for late-M and L-dwarfs, Leggett et al. (2001) noted that below $T_{\mathrm{eff}} < 2500$K, the presence of dust heats the atmosphere in the line-forming region, and the water features may become broader and shallower, depending upon the dust properties (e.g., metallicity). A detailed analysis of such feedback effects between the posited dust layer and the atmosphere are beyond the scope of this investigation.

However, while the blue slope of $K1$ is roughly similar between the L3 and the GPI spectra, the decline seen at the red end of $K2$ deviates sharply from the L3 object spectrum. In comparison, the dereddened spectrum assuming HD 206893 B is similar to an unusually red late field object (L6.5pec) provides a more similar match to the general morphology of K band, with less significant departure from the template object at the longest wavelengths in $K2$. As a slight red slope departure appears to persist after the de-reddening application of a small particle extinction profile, if physical, its origin may be attributed to factors beyond a high-altitude aerosol layer.

Figure 14: Comparison of the full SPHERE+GPI spectrum of HD 206893 B with three late field L-dwarfs (L5: 2MASS J06244595-4521548; L6: 2MASSI J1010148-040649; L7: 2MASSI J0825196+211552). The right panel plots the flux ratios of the standard spectra divided by that of HD 206893 B. The spike at ∼1.55 μm is an artifact corresponding to the gap between the SPHERE IFS band edge and the onset of GPI H-band coverage.
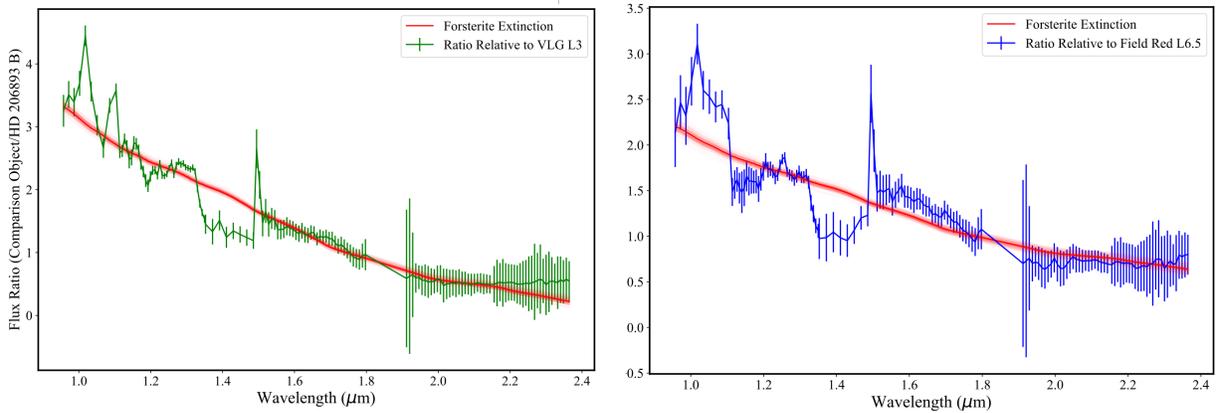

Figure 15: Best-fit forsterite grain aerosol models (red) with the corresponding parameters from the MCMC analysis shown in Figure 16. The green curve represents the observed extinction for HD 206893 B when compared with a VLG L3 object, 2MASSW J2208136+292121 (left panel), and the blue curve for a red field L6.5pec, 2MASSW J2244316+204343 (right panel).
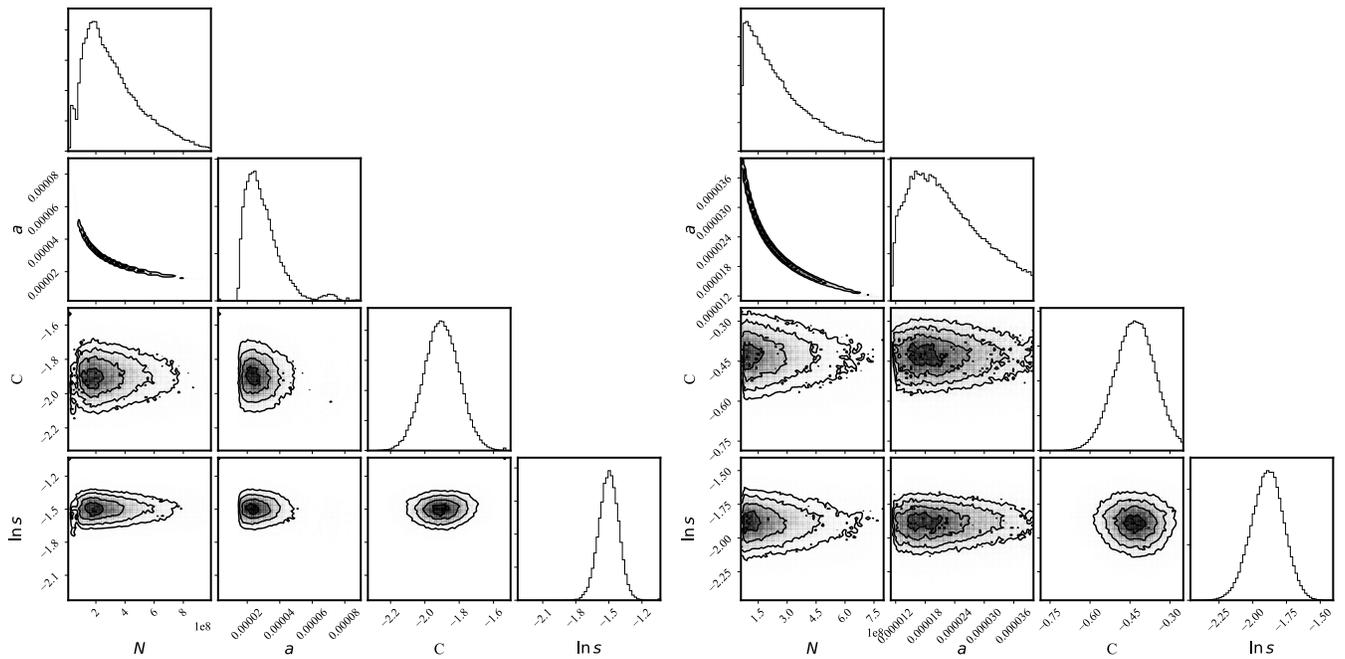
Figure 16: Posterior distributions for the best-fit extinction profiles in Figure 15, with the left panel corresponding to the fit to the assumed L3 extinction profile, and the right panel to the assumed L6.5pec extinction profile. Distributions shown include grain column density in 10^8 particles per cm^2 (N), mean grain size in cm (a), vertical offset due to gray opacity (C) and an error tolerance parameter ($\ln(s)$). The covariance of the mean grain size and column density reflect the inverse proportionality of the parameters, with similar extinction properties for small grain sizes.
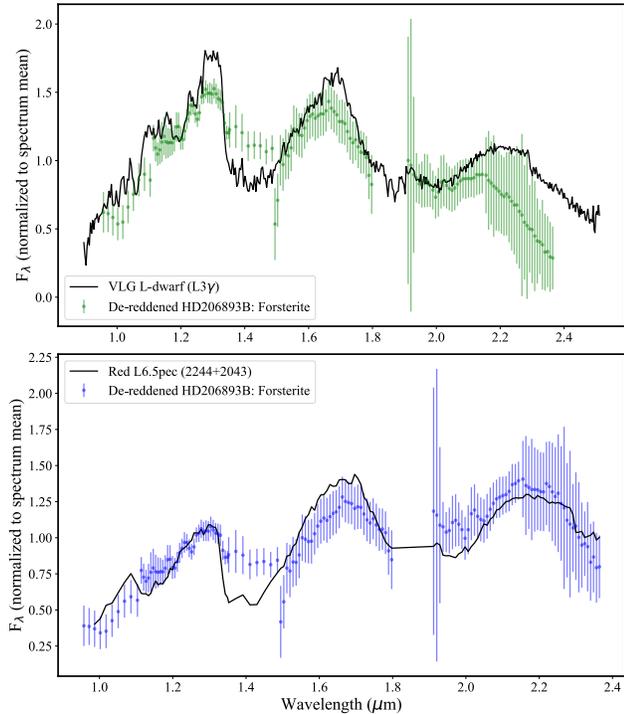
Figure 17: Dereddened spectra of HD 206893 B shown with spectra of a VLG L3 object, 2MASSW J2208136+292121 (top panel) and a red field L6.5pec, 2MASSW J2244316+204343 (bottom panel). The dereddening approach is capable of producing realistic J, H and $K1$-band spectral features in either case, albeit with too shallow H_2O absorption, and is well-approximated by the peaky H-band morphology of the lower surface gravity L3 object. However, the $K2$ band deviates significantly from that of an earlier L-dwarf, and is more similar to that of a late red field object with additional extinction.

6.3. *A possible atmospheric reddening scenario for HD 206893 B*

The high fractional infrared luminosity of HD 206893 A ($L_{dust}/L_* = 2.3 \times 10^{-4}$; Moór et al. 2006) and existence of a companion interior to its debris disk make its architecture similar to companion-disk systems such as HD 95086 ($L_{dust}/L_* = 1.4 \times 10^{-3}$, companion at ~56 au; Chen et al. 2012; Rameau et al. 2016), HR 2562 ($L_{dust}/L_* = 1.1 \times 10^{-4}$, companion at 20 au; Moór et al. 2006; Konopacky et al. 2016), and most recently, HD 193571 ($L_{disk}/L_* = 2.3 \times 10^{-5}$, companion at 11 au; Musso Barcucci et al. 2019). Of these systems, all of which have notably red companions, HD 206893 B remains the reddest, despite the fact that the system does not have the highest fractional infrared luminosity. As described in Section 6.2, additional dust contributions (e.g., in the form of high-altitude aerosols) are necessary to reconcile the spectrum of HD 206893 B with that of field and low-gravity L-dwarfs. Here we examine the plausibility of accretion from the debris disk as a potential source of dusty material in the HD 206893 B atmosphere.

As a simple approximation, the amount of dust required to redden the companion atmosphere can be compared to the debris disk properties derived from previous observations and modeling. We assume that any accreted dust remains solid, and is notfully vaporized during the accretion process[8]. From the derived extinction required to reconcile HD 206893 B's spectrum to that of a VLG L3 object in Section 6.2, the derived column density of $\sim 3 \times 10^8$ cm^{-2} can be used to estimate the excess dust contribution in an aerosol layer. Assuming that the object radius is $1\ R_{\rm Jup}$, and that high-altitude aerosols consist of forsterite particles of size $\sim 0.3\,\mu$m and density 3.27 g/cm^3, suggest the presence of $\sim 9 \times 10^{-10}\ M_{\rm Moon}$ of dust within the atmosphere. Previous analyses of the HD 206893 B debris disk fit the SED with both single and two-component dust temperature models: the two-component dust temperature model included a hot (499 K) dust component at 0.8 au consisting of $1.1 \times 10^{-6}\ M_{\rm Moon}$ of material, and a colder (48 K) dust belt at 261 au of $5.6 \times 10^{-1}\ M_{\rm Moon}$ of material (Chen et al. 2014). The single-component models consisted of a blackbody of 54 K dust at 43 au, with an estimated mass of 0.030 $M_\oplus$ (2.4 $M_{\rm Moon}$) derived from 850 μm JCMT/SCUBA observations (Holland et al. 2017). Adopting a conservative limit of $1.1 \times 10^{-6}\ M_{\rm Moon}$ of hot dust in the inner portion of the disk, we can roughly estimate relative timescales of dust accretion onto the substellar companion.

Accretion rates of solids onto young planets have been estimated at $\sim 10^{-6} M_\oplus$ yr^{-1} for gas-rich disks ($8 \times 10^{-5} M_{\rm Moon}$ yr^{-1}; e.g., Alibert et al. 2018). Assuming this high solid accretion rate, the time required to collect enough material to redden HD 206893 B would be significantly less than one year. However, the HD 206893 debris disk is significantly more evolved, with a much lower dust surface density than younger gas-rich disks. We therefore examine two limiting cases for potential accretion rates: (1) Accretion of solids onto a giant planet based on orbital parameters, and consistent with estimates for younger protoplanetary disks ($10^{-4} M_{\rm disk}$/orbit; Paardekooper 2007), and (2) Estimates of interplanetary dust flux at Jupiter derived from *in situ* measurements from *Pioneer 10* and the *New Horizons* Student Dust Counter (Poppe 2016).

---

[8] We note that the high temperature of an accretion shock similar to those seen in T Tauris could destroy dust, while the ablation and/or vaporization of incident meteoroids is often observed in the Solar System (e.g., on the Earth and Mars; Hunten et al. 1980; Hartwick et al. 2019, respectively), and are thought to seed high-altitude clouds. Also cf. the impact of comet Shoemaker-Levy 9, which produced debris aerosols in the Jovian atmosphere with particle size 0.13–0.3 μm (West et al. 1995).

In the high accretion rate (protoplanetary) scenario, we assume an orbital period of 32 years, as estimated in Section 5.4, a dust mass of $1.1 \times 10^{-6} \, M_{\mathrm{Moon}}$ in the vicinity of the companion (corresponding to the hot dust estimate from Chen et al. 2014), and a solid accretion rate of $10^{-4} M_{\mathrm{disk}}$/orbit, which implies a mass accretion rate of $4 \times 10^{-12} M_{\mathrm{Moon}} \, \mathrm{yr}^{-1}$. Using the derived column density for the companion, this suggests that only a very short period of time ($\sim$260 years) would be required to accrete sufficient dust from the environment and redden the atmosphere to the extent currently observed. In contrast, in the low accretion Solar System-like scenario, typical values of incident dust flux at Jupiter are on the order of $10^{-13} \, \mathrm{g \, m^{-2} \, s^{-1}}$ of 0.5 to $100 \, \mu$m material (Poppe 2016), corresponding to a much lower accretion rate of $6 \times 10^{-16} M_{\mathrm{Moon}} \, \mathrm{yr}^{-1}$ (for a Jovian-sized body), and requiring $\sim$1 Myr to accumulate the estimated dust content in HD 206893 B.

The steady state reached by the atmosphere depends upon the lifetime of the accreted dust, which in turn depends upon the particle-size dependent fall speed and the strength of atmospheric eddy mixing. In lower gravity atmospheres, the fall speed is lower and the effect of a given strength of eddy mixing is stronger, all else being equal, favoring longer dust lifetimes. A complete analysis, accounting for the coupled problems of radiative heating of the atmosphere by the accreted dust and the dust sedimentation, will be considered in the future.

Either of the two accretion scenarios is plausible considering the age of the system and potential replenishment of dust within the disk, and a significantly higher dust estimate at the $\sim$10 au separation of HD 206893 B than the conservative estimate adopted here would increase the interception of grains from the environment into the atmosphere. If the companion is indeed low-surface gravity, sustaining a small dust grain population at high altitude in the atmosphere may be possible for extended periods, particularly if debris disk dust production replenishes the aerosol layer. In comparison to the red colors of the young/low-gravity substellar population, which are already postulated to result from the presence of thick high-altitude clouds, the even redder color of HD 206893 B could potentially be attributed to an additional source of reddening from the dusty disk environment in which it resides.

7. CONCLUSIONS

We present GPI spectroscopy of the substellar companion HD 206893 B, obtained at J, H, $K1$, and $K2$ bands. Consistent with the extraordinary red nature at $H - L'$ initially noted by Milli et al. (2017), the broader spectral coverage of GPI further supports its exceptionally red nature. The overlapping wavelength regimes between the GPI and SPHERE observations shows excellent agreement with the SPHERE YJH observations presented by Delorme et al. (2017). The addition of full H and $K1/K2$ spectroscopy made possible with GPI suggests that the companion may have low surface gravity and that its spectrum appears morphologically most similar to that of the young low-gravity late L-dwarf population.

The GPI photometry of HD 206893 B consistently demonstrates its extraordinary position in color-magnitude space, with $H - Ks = 1.68 \pm 0.08$, significantly redder than the previously reddest substellar object, 2MASS J22362452+4751425 b (2M2236b, $H - K = 1.26 \pm 0.18$, Bowler et al. 2017). From comparison of the GPI spectra to brown dwarf spectral libraries, we find that the closest matching spectrum is that of a late-type, possibly low-gravity L-dwarf, enabling comparison with other extremely red/peculiar objects like 2M2236b ("late-L pec"), 2M1207b (M8.5-L4; Patience et al. 2010), and PSO J318.5-22 (L7; Liu et al. 2013).

We apply a de-reddening approach akin to that of Hiranaka et al. (2016) to determine whether a small grain, sub-micron aerosol layer could reconcile the observed spectrum with that of field and low-gravity L-dwarfs. We find that for reasonable column densities and grain properties, both a low gravity L3 and "peculiar" red field L6.5 provide good matches to HD 206893 B, with the overall spectrum matching that of the later-type object but the spectral shape of features in, e.g., H-band more closely approximated by that of the lower-gravity object.

The emergent spectrum of HD 206893 B proves challenging to fit when conducting comparisons with a suite of various atmospheric model grids, owing to its enhanced luminosity at K-band relative to shorter wavelengths and a slightly unusual $K2$ morphology. Conducting a model grid fit to each of the GPI bands separately provides different companion parameters as compared to fitting the full Y to L spectral coverage of SPHERE, GPI, and NaCo. Each of the four model grids provided more internally consistent effective temperatures for the individual bands (ranging from 1400 K to 1800 K, with an average across all bands and grids of $\sim$1540 K), albeit over the full range of $\log(g)$=3.5–5.0, making the surface gravity of the object ambiguous.

We provide uncertainties on the stellar age ranging from 40-600 Myr, adopting 250 Myr for completeness analyses, but highlight that the high infrared luminosity of the disk and the non-negligible ($61 - 63\%$) likelihood of membership in the Argus association point to a younger age for the system. As the mass of the companion depends on the assumed age, the companion mass ranges from 12-40 M_{Jup} for ages in the $50 - 500$ Myr range of COND models. The peaky morphology of the H band spectra, good fit of the de-reddened spectrum to that of a late-type L-dwarf, morphological similarity of the spectrum to known young moving group late L-dwarfs, and the potential lower dynamical mass of 10 M_{Jup}

estimated by Grandjean et al. (2019), all also point toward a self-consistent scenario for HD 206893 B being significantly younger and lower-mass than initial age estimates and its luminosity have implied.

We have combined the five epochs of VLT astrometry presented in Milli et al. (2017), Delorme et al. (2017), and Grandjean et al. (2019) with four new multiband GPI epochs, spanning four years of orbital coverage. We estimate the orbital period to be $29.1^{+8.1}_{-6.7}$ years, with a probable semi-major axis of $10.4^{+1.8}_{-1.7}$ au and orbital inclination of $145.6^{+13.8}_{-6.6}$ deg. From previous estimates of the debris disk inclination and inner gap radius of $\sim$50 au (Milli et al. 2017), these data are consistent with the companion being well-within the inner edge of the dust emission (as previously suggested by Delorme et al. 2017). The potential significant gap between the $\sim$10 au best-fit semi-major axis and the 50 au inner disk radius has motivated the search for additional companions within the gap. However, no additional companions are detected in our images. The GPI data are 25–75% complete to 5 M$_{\rm Jup}$ at orbital separations of 20-30 au, respectively (assuming an older system age of 250 Myr). If the system is significantly younger, this may suggest that any additional companion responsible for carving the disk edge would be sub-Jovian. Comparing our MCMC fits to the visual orbit with the initial disk geometry estimates from Milli et al. (2017) favors less misaligned and more co-planar orbital configurations; however, the measurement precision on disk and orbital elements cannot currently exclude moderately misaligned ($i_m \sim 20°$) configurations. As recent work has shown that i_m correlates with the orbital period of companions in circumbinary systems (Czekala et al. 2019), with tighter binaries exhibiting greater coplanarity, this system provides a useful laboratory for disk-companion dynamics. Milli et al. (2017) caveat that the marginally-resolved nature of the debris disk from 70 μm *Herschel* observations do not tightly constrain the disk geometry, necessitating future disk observations at higher spatial resolution and longer-term orbital monitoring to explore the dynamical interplay between the companion and disk environment.

As the reddest substellar companion identified to date, HD 206893 B adds to the growing population of remarkably red planetary mass objects and free-floating objects. With its exceptional color and close orbital separation, HD 206893 B is an important comparison for similarly red free-floating objects (e.g., PSO 318), red, wide substellar objects like 2M2236b, and planetary-mass companions posited to have high photospheric dust content like HD 95086 b (De Rosa et al. 2016). The redness of the companion and its extremely dusty nature also make it well-suited to exploring the effects of clouds, metallicity, and disequilibrium chemistry at cool temperatures in atmospheric models. Interpreting these observations, and future observations extended further into the infrared (e.g., with the *James Webb Space Telescope*), will likely be subject to how dusty clouds, collisionally-induced absorption, and atmospheric chemistry are treated in models (Baudino et al. 2017), and unusual systems such as HD 206893 B will provide important laboratories for these processes. **Furthermore, if the system is indeed young, this companion would present an exceptional addition to the growing population of directly-imaged giant exoplanets.** If the system is $\sim$250 Myr, HD 206893 B represents only the second detection of a brown dwarf orbiting within the inner gap of its host debris disk (after HR 2562; Konopacky et al. 2016), and is otherwise one of only six substellar companion systems with both resolved disks and companions. This makes it a key testing ground to explore dynamical interaction between disks, companions, and their host stars. The dustiness of the system also merits a search for polarized signal from the companion (e.g., as observed in companion systems like CT Cha and HD 142527; Ginski et al. 2018; Rodigas et al. 2014). With multi-wavelength spectral coverage, detailed modeling, and continued dynamical monitoring, constraining the physical properties of this system will provide critical context for our understanding of the atmospheric and evolutionary histories of substellar objects.

APPENDIX

A. PIPELINE POST-PROCESSING AND COVARIANCE ESTIMATION

A.1. *pyKLIP Reduction*

The images from the GPI auto-reduced pyKLIP pipeline (Wang et al. 2018) are shown in Figure 18, with reduction parameters of nine annuli, four subsections per annulus, and exclusion criterion corresponding to movement of one pixel, using the first 10 KL modes to generate the reference PSF. The images show the close separation of the companion to the coronagraphic mask.
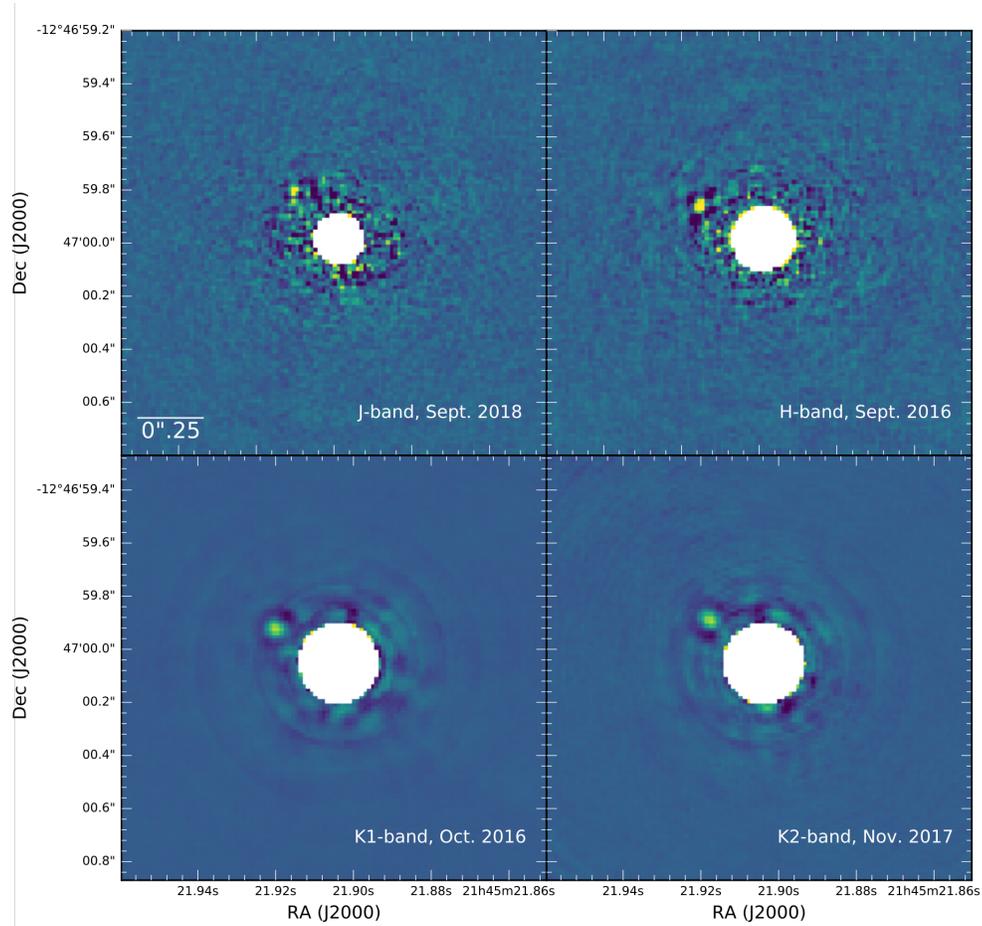
Figure 18: Auto-reduced and pipeline-processed PSF-subtracted images of HD 206893 B in J-band (upper left), H-band (upper right), $K1$-band (lower left), and $K2$-band (lower right). Images shown are from the pyKLIP reductions, oriented north up and east left, with parameters of 9 annuli, 4 subsections, 1 pixel movement criterion, and using the first 10 KL modes. Each individual image is scaled separately to minimize the contributions of residual speckle noise. Noticeable change in the companion position angle can be seen between the earliest 2016 epoch (upper right) and the latest 2018 epoch (upper left).

A.2. *K2 Spectral Extraction*

As noted in Section 5.2, the red end of the GPI $K2$ spectrum shows a steep spectral slope beyond 2.2μm. This slope was observed in both epochs of $K2$ data taken one year apart, and appears to be affected predominantly by the very low SNR in the GPI satellite spots at the red end of the band, which are critical to calibrate the measured flux in individual frames. The spectral slope is also impacted by the excessive brightness of the companion in these frames, the flux of which was significantly altered by the narrow high pass filter. Therefore, the shape of the extracted spectrum varies significantly depending upon decisions made in post-processing and PSF subtraction. We show the results of the 2016 CADI extraction in Figure 19, keeping in mind the strong bias of this spectrum due to very low SNR of the satellite spots, compared with the 2017 CADI and LOCI extractions with a high pass filter of 4 equivalent-pixels. Reducing the 2016 dataset with both LOCI and a broader high pass filter resulted in the same spectrum as with cADI and a narrow filter (4 pixels). The 2017 epoch of data has higher SNR owing to significantly more field rotation and longer integration, and because LOCI performed with a moderately large high-pass filter (10 pixels) recovers more flux from the extended wings of the PSF in the redder channels, we use the LOCI extraction throughout the analysis in this study.
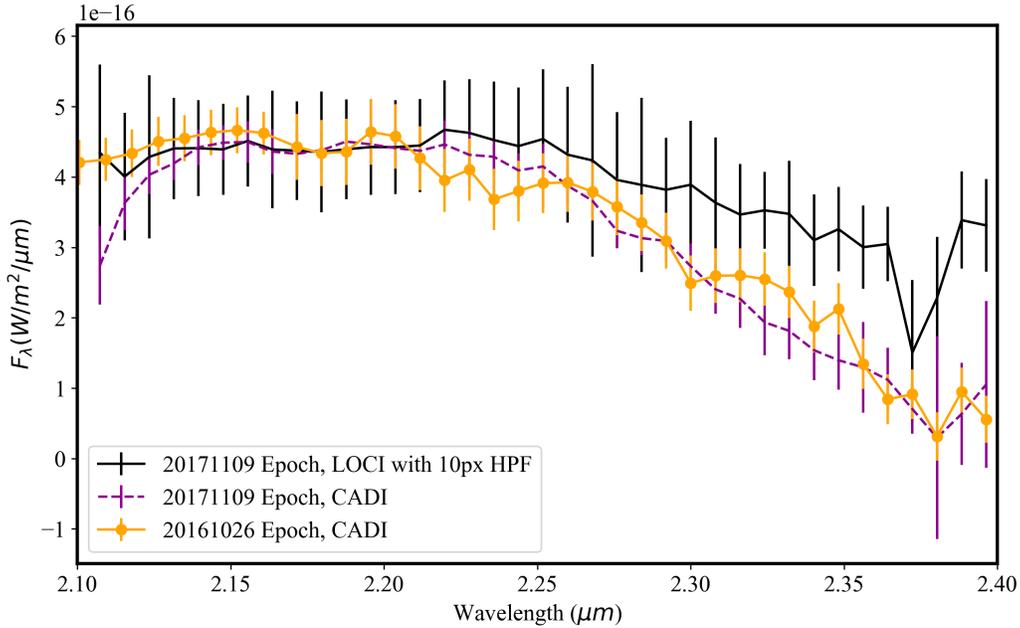
Figure 19: Comparisons of post-processing approaches for the GPI $K2$-band data, demonstrating the recovery of flux at longer wavelengths. The 2017-11-09 LOCI extraction (black line) with a broader high pass filter is used in this study.

A.3. *Covariance Estimation*

Figure 20 shows the spectral covariance matrices, derived from measuring inter-pixel correlation within the final PSF-subtracted LOCI and cADI images. Each covariance matrix was calculated independently for each GPI band by use of a parallel-tempered MCMC to fit the 18-parameters of spectral correlation in the IFS datacubes as outlined in Greco & Brandt (2016) and applied in De Rosa et al. (2016). Each MCMC was run with 128 walkers at 16 different temperatures and run for 5000 steps saving every tenth step, burning-in the first 1000 steps in the chains. Plotted are the spectral correlations as a function of wavelength channel for the final datacube in each GPI band, where the off-diagonal elements correspond to correlated noise terms. For each spectrum, the high and low-frequency noise components, corresponding to read/background noise and speckle noise, respectively, are extracted and introduced into the error budget of the final spectra separately. Table 5 provides the fitted amplitudes of the correlated noise terms with respect to angular separation (A_ρ) and with respect to wavelength due to interpolation or crosstalk (A_λ). Detailed results from applying the spectral covariance to model fitting of the spectra are provided in Sections 5.3 and B.

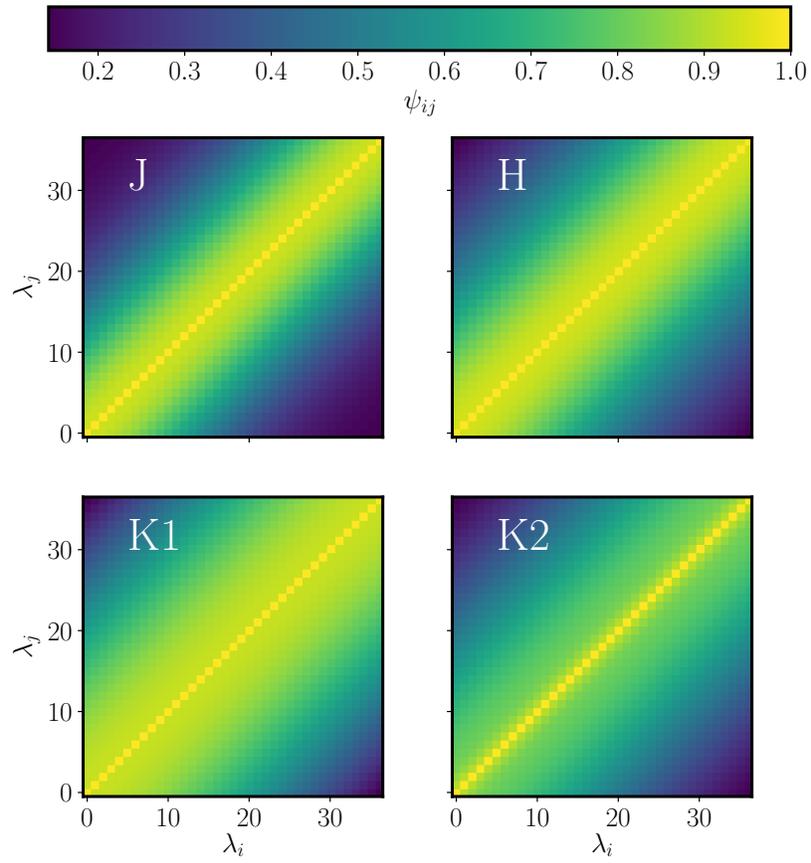**Figure 20**: Spectral correlation matrices calculated from the LOCI and cADI PSF-subtracted datacubes, with the correlation between pixel values at different wavelength slices shown as intensity. The greatest spectral covariance can be seen at H and $K1$ bands, with broad off-diagonal terms corresponding to high correlation between adjacent wavelength channels.

Band	ρ (mas)	A_ρ	A_λ
J (σ_ρ=0.51, σ_λ=4.05)	200	0.70	0.25
	225	0.80	0.14
	250	0.57	0.33
	265	0.51	0.38
	280	0.75	0.14
	300	0.89	0.02
	325	0.89	0.01
	350	0.86	0.01
H (σ_ρ=1.14, σ_λ=0.07)	200	0.59	0.37
	225	0.60	0.34
	250	0.56	0.39
	265	0.70	0.23
	280	0.68	0.25
	300	0.55	0.37
	325	0.37	0.51
	350	0.04	0.81
K1 (σ_ρ=0.37, σ_λ=0.13)	200	0.02	0.93
	225	0.73	0.18
	250	0.73	0.14
	265	0.63	0.22
	280	0.66	0.16
	300	0.74	0.01
	325	0.64	0.05
	350	0.63	0.01
K2 (σ_ρ=0.31, σ_λ=0.01)	200	0.83	0.10
	225	0.82	0.10
	250	0.79	0.10
	265	0.78	0.10
	280	0.77	0.08
	300	0.65	0.17
	325	0.54	0.22
	350	0.51	0.26

Table 5: Measured amplitudes of the correlated noise terms for each GPI datacube (A_ρ and A_λ), with the relevant correlation lengths measured for each band (σ_ρ, σ_λ). The separations within the datacube are selected to span the range of companion separations at various epochs of observation.

Model Grid	Range	Standard χ^2 Fitting				Fitting Incorporating Covariance			
		T_{Eff} (K)	log(g)	Radius (R_{Jup})	χ^2	T_{Eff} (K)	log(g)	Radius (R_{Jup})	χ^2
Sonora	Full	1100	5.0	1.68	4.4	1200	5.0	1.36	3.5
	J	1200	5.0	1.19	0.3	1400	5.0	0.82	1.4
	H	1300	3.7	1.06	0.9	1400	3.7	1.13	1.4
	K1	1400	3.7	1.28	0.2	1400	3.7	1.28	2.7
	K2	1400	3.7	1.28	0.2	1500	3.7	1.18	0.7
CloudyAE-60	Full	1200	3.5	1.67	4.4	1700	3.5	1.55	8.6
	J	1700	3.5	1.31	1.8	1700	3.5	1.25	5.2
	H	1400	3.5	2.56	2.0	1700	3.5	1.77	2.4
	K1	1700	3.5	2.68	0.5	1700	3.5	2.82	7.3
	K2	1700	3.5	2.77	0.2	1700	3.5	2.80	1.1
DRIFT-PHOENIX	Full	1400	4.5	1.68	0.8	1400	4.5	1.36	1.2
	J	1400	3.0	1.23	0.1	1500	4.5	1.33	0.9
	H	1100*	5.0	3.01	0.2	1400	3.0	1.34	0.9
	K1	1800*	3.0	0.81	0.2	1800*	3.5	0.80	2.5
	K2	2000	5.0	0.71	0.2	1300*	5.0	1.63	0.6
BT-Settl	Full	1600	3.5	0.94	1.6	1600	3.5	0.96	1.2
	J	1600	3.5	0.91	0.1	1600	3.5	0.88	0.9
	H	1600	3.5	0.87	0.3	1500	3.0	1.12	1.1
	K1	1800	4.5	0.76	0.1	1700	4.0	0.80	2.2
	K2	1700	4.5	0.83	0.2	1500	3.5	1.28	0.7

Table 6: Best-fit model properties for each of the four suites of models, both using a standard χ^2 minimization (visualized in Figure 9) and when incorporating covariance matrices. Asterisks (*) indicate best-fit models from DRIFT-PHOENIX with super-solar metallicity ($[M/H] = +0.3$).

B. DETAILED RESULTS FOR MODEL ATMOSPHERIC GRIDS

B.1. *Modeling Results With and Without Covariances*

Section 5.3 describes the modeling results implementing spectral covariance as summarized in Figure 20 and Table 5, and here we provide additional details on each of the model grids explored in the fitting of the HD 206893 B spectrum and the results from a standard χ^2 minimization. Table 6 summarizes the properties of the best fit models to the full spectrum and all four bands, demonstrating the wide range of derived physical properties dependent upon the wavelength range, choice of models, and whether or not covariances were implemented. As noted in Section 5.3, the best fit models accounting for spectral covariances do not always pass through the spectral datapoints in cases where the spectra are highly correlated; however, the resulting derived parameters across all four bands using covariances agree more closely than the wider range of temperatures, surface gravities, and radii estimated from a standard χ^2 minimization.

B.2. *Model Descriptions*

Sonora Models: We conducted model comparisons with a subset of cloudy, solar-metallicity models from the upcoming Sonora 2020 model grid (Marley et al. 2020, in prep.). The Sonora models are applicable to brown dwarfs and giant exoplanets and incorporate revised solar abundances (Lodders 2010), rainout chemistry, updated opacities for H_2, CH_4 and alkali species, equilibrium and disequilibrium chemistry, and span both cloudless and cloudy models with temperatures of 200–2400 K and metallicities of $-0.5 \leq [M/H] \leq 2$. The subset of solar metallicity cloudy models tested here span T_{eff}=1100–1600 K and log(g)=3.75–5.0. The cloudy Sonora models use the cloud model of Ackerman & Marley (2001) which is parametrized by the grain sedimentation efficiency, f_{sed}. This parameter sets the balance between grain sedimentation and upward motion from turbulent mixing. Small values of f_{sed} correspond to slow sedimentation, smaller grains, and vertically extended clouds. The value of f_{sed} was set equal to 1 (moderate particle settling efficiency) in the tested model subset, corresponding to a vertically extended thick cloud layer. Fitting over the full wavelength range favors a very low temperature 1200 K object with high surface gravity, and a physically-plausible radius of $\sim$1.36R_{Jup}. The results from fitting individual bands favor slightly higher temperatures and generally lower surface gravities, suggesting that the low temperature over the full wavelength range is driven by both spectral correlation and increasing redness in the relative band-to-band flux. These models more closely approximate the

emergent flux across shorter wavelengths and the shallow water absorption features between J and H, but underestimate the flux at the longest wavelengths.

DRIFT-PHOENIX Models: We also compared the spectra of HD 206893 B with the DRIFT-PHOENIX Atmosphere Models, which incorporate small grains in their mineral cloud physics prescription. The DRIFT-PHOENIX models are built upon the PHOENIX radiative transfer atmosphere models (Hauschildt 1992), but also incorporate microparticle physics through the DRIFT code (Dehn et al. 2007; Helling et al. 2008; Witte et al. 2009), which includes the motion of particles within forming clouds and treats a variety of particle sizes and compositions. The DRIFT-PHOENIX models tested range from T_{eff}=1000–3000 K, $\log(g)$=3.0–6.0, and metallicities of solar $[M/H]$=0 or +0.3 (super-solar). For model comparisons with DRIFT-PHOENIX, solar metallicity models generally produced better fits than super-solar, concordant with the metallicity estimate for HD 206893 A from Delorme et al. (2017); only two individual GPI bands were best-fit with $[M/H]$=+0.3 in either the standard χ^2 or covariance fitting. The best model fit to the full spectrum favors a moderate temperature (1400 K) and surface gravity ($\log(g)$ = 4.5), and plausible object radius (1.36R$_{\rm Jup}$). The DRIFT-PHOENIX best-fit model most closely reproduces the general rise in flux from the bluest to reddest wavelengths in this study but underestimates the flux over K, in addition to shallower water absorption and overestimation of the L' photometry.

Cloudy-AE60 (Madhusudhan et al. 2011) Models: Given the red nature of the companion, we fit its spectra with the publicly-available cloudy atmosphere models generated by Madhusudhan et al. (2011) for the HR 8799 planets, which are also anomalously red relative to the field population. The full model grid includes both cloudy and cloud-free atmospheres with a range of forsterite cloud thicknesses and optical depths. The Madhusudhan et al. (2011) modal grain sizes for the cloudy atmospheres are in the $60\,\mu$m size range (although similar results can be achieved within these models for $\sim1\,\mu$m Fe grains at 1% super saturation, demonstrating some degeneracies in opacity that depend upon composition and grain size). Due to the red nature of HD 206893 B, we focus on the Cloudy-AE grid, which has the greatest vertical extent in cloud depth; this generally serves to suppress emergent flux at shorter wavelengths and produce higher fluxes at longer wavelengths for the same effective temperature. However, we find that the best fit model incorporating covariances corresponds to low surface gravity ($\log(g)$=3.5) and the hottest temperature (1700 K) of the four grids, but is remarkably consistent across the four separate band-to-band fits. The full spectral fit corresponds to a model which is significantly bluer than that of HD 206893 B, with the largest estimated corresponding radius (1.55 R$_{\rm Jup}$).

BT-Settl Models: The wide range of potential masses and temperatures for the companion estimated by the other model grids motivates further spectral comparison with the BT-Settl (2015) models (Allard et al. 2012; Allard 2014), which cover larger ranges in these values. BT-Settl was designed to model the atmospheres of very low-mass stars, brown dwarfs, and planets using the PHOENIX radiative transfer atmosphere models (Hauschildt 1992) in conjunction with updated molecular line lists for water, methane, ammonia, and CO$_2$, and revised solar abundances derived from the solar radiative hydrodynamical simulations from Asplund et al. (2009). The BT-Settl models include a cloud treatment involving supersaturation, which accounts for cloud growth and mixing, and aims to reproduce the stellar M-L and brown dwarf L-T transitions. To conduct a comparison with the HD 206893 B spectra, and given the likely solar metallicity of the host star, we use the solar metallicity BT-Settl (2015) models with grid parameters ranging from 1200 K to 2050 K and surface gravities ranging from $\log(g)$=2.5–5.5. The resulting best-fit full spectral model shown in Figure 9 corresponds to T$_{\rm eff}$ of 1600 K, a low surface gravity ($\log(g)$=3.5), and a radius of 0.96 R$_{\rm Jup}$. Along with the best-fit DRIFT-PHOENIX model, this fit has the lowest reduced χ^2 incorporating spectral covariance. This model reproduces flux over the YJ bands well, and most closely approximates the L' photometry of all four model suites, but is insufficiently red and departs significantly from the K spectra.

REFERENCES

Abrahams, E., & Cruz, K. 2017, BDNYC/UltracoolTypingKit:
    UltracoolTypingKit v1.0.0, doi: 10.5281/zenodo.840582

Ackerman, A. S., & Marley, M. S. 2001, ApJ, 556, 872,
    doi: 10.1086/321540

Alibert, Y., Venturini, J., Helled, R., et al. 2018, Nature Astronomy,
    2, 873, doi: 10.1038/s41550-018-0557-2

Allard, F. 2014, in IAU Symposium, Vol. 299, Exploring the
    Formation and Evolution of Planetary Systems, ed. M. Booth,
    B. C. Matthews, & J. R. Graham, 271–272,
    doi: 10.1017/S1743921313008545

Allard, F., Hauschildt, P. H., Alexander, D. R., Tamanai, A., &
    Schweitzer, A. 2001, ApJ, 556, 357, doi: 10.1086/321547

Allard, F., Homeier, D., & Freytag, B. 2012, Philosophical
    Transactions of the Royal Society of London Series A, 370,
    2765, doi: 10.1098/rsta.2011.0269

Allers, K. N., & Liu, M. C. 2013, ApJ, 772, 79,
    doi: 10.1088/0004-637X/772/2/79

Asplund, M., Grevesse, N., Sauval, A. J., & Scott, P. 2009,
    ARA&A, 47, 481,
    doi: 10.1146/annurev.astro.46.060407.145222

Bailey, V., Meshkat, T., Reiter, M., et al. 2014, ApJL, 780, L4, doi: 10.1088/2041-8205/780/1/L4

Baraffe, I., Chabrier, G., Allard, F., & Hauschildt, P. H. 2002, A&A, 382, 563, doi: 10.1051/0004-6361:20011638

Baraffe, I., Chabrier, G., Barman, T. S., Allard, F., & Hauschildt, P. H. 2003, A&A, 402, 701, doi: 10.1051/0004-6361:20030252

Baraffe, I., Homeier, D., Allard, F., & Chabrier, G. 2015, A&A, 577, A42, doi: 10.1051/0004-6361/201425481

Baudino, J.-L., Mollière, P., Venot, O., et al. 2017, ApJ, 850, 150, doi: 10.3847/1538-4357/aa95be

Bell, C. P. M., Mamajek, E. E., & Naylor, T. 2015, MNRAS, 454, 593, doi: 10.1093/mnras/stv1981

Beuzit, J.-L., Feldt, M., Dohlen, K., et al. 2008, in Proc. SPIE, Vol. 7014, Ground-based and Airborne Instrumentation for Astronomy II, 701418, doi: 10.1117/12.790120

Bowler, B. P. 2016, PASP, 128, 102001, doi: 10.1088/1538-3873/128/968/102001

Bowler, B. P., Liu, M. C., Mawet, D., et al. 2017, AJ, 153, 18, doi: 10.3847/1538-3881/153/1/18

Burgasser, A. J., Geballe, T. R., Leggett, S. K., Kirkpatrick, J. D., & Golimowski, D. A. 2006, ApJ, 637, 1067, doi: 10.1086/498563

Burgasser, A. J., & the SPLAT Development Team. 2017, ArXiv e-prints. https://arxiv.org/abs/1707.00062

Burrows, A., Hubbard, W. B., Lunine, J. I., & Liebert, J. 2001, Reviews of Modern Physics, 73, 719, doi: 10.1103/RevModPhys.73.719

Caffau, E., Ludwig, H. G., Steffen, M., Freytag, B., & Bonifacio, P. 2011, SoPh, 268, 255, doi: 10.1007/s11207-010-9541-4

Cardelli, J. A., Clayton, G. C., & Mathis, J. S. 1989, ApJ, 345, 245, doi: 10.1086/167900

Chen, C. H., Mittal, T., Kuchner, M., et al. 2014, ApJS, 211, 25, doi: 10.1088/0067-0049/211/2/25

Chen, C. H., Pecaut, M., Mamajek, E. E., Su, K. Y. L., & Bitner, M. 2012, ApJ, 756, 133, doi: 10.1088/0004-637X/756/2/133

Choi, J., Dotter, A., Conroy, C., et al. 2016, ApJ, 823, 102, doi: 10.3847/0004-637X/823/2/102

Cruz, K. L., Núñez, A., Burgasser, A. J., et al. 2018, AJ, 155, 34, doi: 10.3847/1538-3881/aa9d8a

Czekala, I., Chiang, E., Andrews, S. M., et al. 2019, arXiv e-prints, arXiv:1906.03269. https://arxiv.org/abs/1906.03269

Dahn, C. C., Harris, H. C., Vrba, F. J., et al. 2002, AJ, 124, 1170, doi: 10.1086/341646

David, T. J., & Hillenbrand, L. A. 2015, ApJ, 804, 146, doi: 10.1088/0004-637X/804/2/146

De Rosa, R. J., Nielsen, E. L., Blunt, S. C., et al. 2015, ApJL, 814, L3, doi: 10.1088/2041-8205/814/1/L3

De Rosa, R. J., Rameau, J., Patience, J., et al. 2016, ApJ, 824, 121, doi: 10.3847/0004-637X/824/2/121

Dehn, M., Helling, C., Woitke, P., & Hauschildt, P. 2007, in IAU Symposium, Vol. 239, Convection in Astrophysics, ed. F. Kupka, I. Roxburgh, & K. L. Chan, 227–229, doi: 10.1017/S1743921307000488

Delorme, P., Schmidt, T., Bonnefoy, M., et al. 2017, A&A, 608, A79, doi: 10.1051/0004-6361/201731145

Dohlen, K., Langlois, M., Saisse, M., et al. 2008, in Proc. SPIE, Vol. 7014, Ground-based and Airborne Instrumentation for Astronomy II, 70143L, doi: 10.1117/12.789786

Dotter, A. 2016, ApJS, 222, 8, doi: 10.3847/0067-0049/222/1/8

Dupuy, T. J., & Kraus, A. L. 2013, Science, 341, 1492, doi: 10.1126/science.1241917

Dupuy, T. J., & Liu, M. C. 2012, ApJS, 201, 19, doi: 10.1088/0067-0049/201/2/19

Faherty, J. K., Rice, E. L., Cruz, K. L., Mamajek, E. E., & Núñez, A. 2013, AJ, 145, 2, doi: 10.1088/0004-6256/145/1/2

Faherty, J. K., Riedel, A. R., Cruz, K. L., et al. 2016, ApJS, 225, 10, doi: 10.3847/0067-0049/225/1/10

Filippazzo, J. C., Rice, E. L., Faherty, J., et al. 2015, ApJ, 810, 158, doi: 10.1088/0004-637X/810/2/158

Fitzpatrick, E. L. 1999, PASP, 111, 63, doi: 10.1086/316293

Foreman-Mackey, D., Hogg, D. W., Lang, D., & Goodman, J. 2013, PASP, 125, 306, doi: 10.1086/670067

Gagné, J., Lafrenière, D., Doyon, R., Malo, L., & Artigau, É. 2014, ApJ, 783, 121, doi: 10.1088/0004-637X/783/2/121

Gagné, J., Faherty, J. K., Cruz, K. L., et al. 2015, ApJS, 219, 33, doi: 10.1088/0067-0049/219/2/33

Gagné, J., Mamajek, E. E., Malo, L., et al. 2018, ApJ, 856, 23, doi: 10.3847/1538-4357/aaae09

Gaia Collaboration, Brown, A. G. A., Vallenari, A., et al. 2018, A&A, 616, A1, doi: 10.1051/0004-6361/201833051

Galicher, R., Marois, C., Macintosh, B., et al. 2016, A&A, 594, A63, doi: 10.1051/0004-6361/201527828

Ginski, C., Benisty, M., van Holstein, R. G., et al. 2018, A&A, 616, A79, doi: 10.1051/0004-6361/201732417

Gizis, J. E., Faherty, J. K., Liu, M. C., et al. 2012, AJ, 144, 94, doi: 10.1088/0004-6256/144/4/94

Grandjean, A., Lagrange, A. M., Beust, H., et al. 2019, arXiv e-prints, arXiv:1906.02058. https://arxiv.org/abs/1906.02058

Greco, J. P., & Brandt, T. D. 2016, ApJ, 833, 134, doi: 10.3847/1538-4357/833/2/134

Güver, T., & Özel, F. 2009, MNRAS, 400, 2050, doi: 10.1111/j.1365-2966.2009.15598.x

Hartwick, V. L., Toon, O. B., & Heavens, N. G. 2019, Nature Geoscience, 12, 516, doi: 10.1038/s41561-019-0379-6

Hauschildt, P. H. 1992, JQSRT, 47, 433, doi: 10.1016/0022-4073(92)90105-D

Helling, C., Woitke, P., & Thi, W.-F. 2008, A&A, 485, 547, doi: 10.1051/0004-6361:20078220

Hiranaka, K., Cruz, K. L., Douglas, S. T., Marley, M. S., & Baldassare, V. F. 2016, ApJ, 830, 96, doi: 10.3847/0004-637X/830/2/96

Holland, W. S., Matthews, B. C., Kennedy, G. M., et al. 2017, MNRAS, 470, 3606, doi: 10.1093/mnras/stx1378

Hunten, D. M., Turco, R. P., & Toon, O. B. 1980, Journal of Atmospheric Sciences, 37, 1342, doi: 10.1175/1520-0469(1980)037⟨1342:SADPOM⟩2.0.CO;2

Johnson-Groh, M., Marois, C., De Rosa, R. J., et al. 2017, AJ, 153, 190, doi: 10.3847/1538-3881/aa6480

Kalas, P., Graham, J. R., Chiang, E., et al. 2008, Science, 322, 1345, doi: 10.1126/science.1166609

Kellogg, K., Metchev, S., Gagné, J., & Faherty, J. 2016, ApJL, 821, L15, doi: 10.3847/2041-8205/821/1/L15

Kellogg, K., Metchev, S., Geißler, K., et al. 2015, AJ, 150, 182, doi: 10.1088/0004-6256/150/6/182

Kellogg, K., Metchev, S., Miles-Páez, P. A., & Tannock, M. E. 2017, AJ, 154, 112, doi: 10.3847/1538-3881/aa83b0

Keppler, M., Benisty, M., Müller, A., et al. 2018, A&A, 617, A44, doi: 10.1051/0004-6361/201832957

Kirkpatrick, J. D., Reid, I. N., Liebert, J., et al. 2000, AJ, 120, 447, doi: 10.1086/301427

Kirkpatrick, J. D., Looper, D. L., Burgasser, A. J., et al. 2010, ApJS, 190, 100, doi: 10.1088/0067-0049/190/1/100

Kirkpatrick, J. D., Cushing, M. C., Gelino, C. R., et al. 2011, ApJS, 197, 19, doi: 10.1088/0067-0049/197/2/19

Kitzmann, D., & Heng, K. 2018, MNRAS, 475, 94, doi: 10.1093/mnras/stx3141

Konopacky, Q. M., Thomas, S. J., Macintosh, B. A., et al. 2014, in Proc. SPIE, Vol. 9147, Ground-based and Airborne Instrumentation for Astronomy V, 914784, doi: 10.1117/12.2056646

Konopacky, Q. M., Rameau, J., Duchêne, G., et al. 2016, ApJL, 829, L4, doi: 10.3847/2041-8205/829/1/L4

Kraus, A. L., & Ireland, M. J. 2012, ApJ, 745, 5, doi: 10.1088/0004-637X/745/1/5

Lafrenière, D., Marois, C., Doyon, R., Nadeau, D., & Artigau, É. 2007, ApJ, 660, 770, doi: 10.1086/513180

Lagrange, A. M., Bonnefoy, M., Chauvin, G., et al. 2010, Science, 329, 57, doi: 10.1126/science.1187187

Lee, J., & Song, I. 2019, MNRAS, 486, 3434, doi: 10.1093/mnras/stz1044

Leggett, S. K., Allard, F., Geballe, T. R., Hauschildt, P. H., & Schweitzer, A. 2001, ApJ, 548, 908, doi: 10.1086/319020

Leggett, S. K., Golimowski, D. A., Fan, X., Geballe, T. R., & Knapp, G. R. 2003, in Cambridge Workshop on Cool Stars, Stellar Systems, and the Sun, Vol. 12, The Future of Cool-Star Astrophysics: 12th Cambridge Workshop on Cool Stars, Stellar Systems, and the Sun, ed. A. Brown, G. M. Harper, & T. R. Ayres, 120–127

Liu, M. C., Dupuy, T. J., & Allers, K. N. 2016, ApJ, 833, 96, doi: 10.3847/1538-4357/833/1/96

Liu, M. C., Magnier, E. A., Deacon, N. R., et al. 2013, ApJL, 777, L20, doi: 10.1088/2041-8205/777/2/L20

Lodders, K. 2010, Astrophysics and Space Science Proceedings, 16, 379, doi: 10.1007/978-3-642-10352-0_8

Looper, D. L., Kirkpatrick, J. D., Cutri, R. M., et al. 2008, ApJ, 686, 528, doi: 10.1086/591025

Macintosh, B., Graham, J. R., Ingraham, P., et al. 2014, Proceedings of the National Academy of Science, 111, 12661, doi: 10.1073/pnas.1304215111

Macintosh, B. A., Graham, J. R., Palmer, D. W., et al. 2008, in Proc. SPIE, Vol. 7015, Adaptive Optics Systems, 701518, doi: 10.1117/12.788083

Madhusudhan, N., Burrows, A., & Currie, T. 2011, ApJ, 737, 34, doi: 10.1088/0004-637X/737/1/34

Maire, J., Ingraham, P. J., De Rosa, R. J., et al. 2014, in Proc. SPIE, Vol. 9147, Ground-based and Airborne Instrumentation for Astronomy V, 914785, doi: 10.1117/12.2056732

Manjavacas, E., Bonnefoy, M., Schlieder, J. E., et al. 2014, A&A, 564, A55, doi: 10.1051/0004-6361/201323016

Marley, M., Saumon, D., Morley, C., & Fortney, J. 2018, Sonora 2018: Cloud-free, solar composition, solar C/O substellar atmosphere models and spectra, doi: 10.5281/zenodo.1309035

Marley, M. S., Saumon, D., Cushing, M., et al. 2012, ApJ, 754, 135, doi: 10.1088/0004-637X/754/2/135

Marocco, F., Day-Jones, A. C., Lucas, P. W., et al. 2014, MNRAS, 439, 372, doi: 10.1093/mnras/stt2463

Marois, C., Lafrenière, D., Doyon, R., Macintosh, B., & Nadeau, D. 2006a, ApJ, 641, 556, doi: 10.1086/500401

Marois, C., Lafrenière, D., Macintosh, B., & Doyon, R. 2006b, ApJ, 647, 612, doi: 10.1086/505191

Marois, C., Macintosh, B., Barman, T., et al. 2008, Science, 322, 1348, doi: 10.1126/science.1166585

Marois, C., Macintosh, B., & Véran, J.-P. 2010, in Proc. SPIE, Vol. 7736, Adaptive Optics Systems II, 77361J, doi: 10.1117/12.857225

Matthews, B. C., Kennedy, G., Sibthorpe, B., et al. 2015, ApJ, 811, 100, doi: 10.1088/0004-637X/811/2/100

Mawet, D., Riaud, P., Absil, O., & Surdej, J. 2005, ApJ, 633, 1191, doi: 10.1086/462409

Mawet, D., David, T., Bottom, M., et al. 2015, ApJ, 811, 103, doi: 10.1088/0004-637X/811/2/103

McLean, I. S., McGovern, M. R., Burgasser, A. J., et al. 2003, ApJ, 596, 561, doi: 10.1086/377636

Milli, J., Hibon, P., Christiaens, V., et al. 2017, A&A, 597, L2, doi: 10.1051/0004-6361/201629908

Moór, A., Ábrahám, P., Derekas, A., et al. 2006, ApJ, 644, 525, doi: 10.1086/503381

Morzinski, K. M., Males, J. R., Skemer, A. J., et al. 2015, ApJ,
    815, 108, doi: 10.1088/0004-637X/815/2/108

Musso Barcucci, A., Launhardt, R., Kennedy, G. M., et al. 2019,
    arXiv e-prints, arXiv:1906.01391.
    https://arxiv.org/abs/1906.01391

Nielsen, E. L., Rosa, R. J. D., Rameau, J., et al. 2017, AJ, 154, 218,
    doi: 10.3847/1538-3881/aa8a69

Nielsen, E. L., De Rosa, R. J., Macintosh, B., et al. 2019, AJ, 158,
    13, doi: 10.3847/1538-3881/ab16e9

Paardekooper, S. J. 2007, A&A, 462, 355,
    doi: 10.1051/0004-6361:20066326

Patience, J., King, R. R., de Rosa, R. J., & Marois, C. 2010, A&A,
    517, A76, doi: 10.1051/0004-6361/201014173

Perrin, M. D., Ingraham, P., Follette, K. B., et al. 2016, in
    Proc. SPIE, Vol. 9908, Ground-based and Airborne
    Instrumentation for Astronomy VI, 990837,
    doi: 10.1117/12.2233197

Poppe, A. R. 2016, Icarus, 264, 369,
    doi: 10.1016/j.icarus.2015.10.001

Rajan, A., Rameau, J., De Rosa, R. J., et al. 2017, AJ, 154, 10,
    doi: 10.3847/1538-3881/aa74db

Rameau, J., Nielsen, E. L., De Rosa, R. J., et al. 2016, ApJL, 822,
    L29, doi: 10.3847/2041-8205/822/2/L29

Rieke, G. H., & Lebofsky, M. J. 1985, ApJ, 288, 618,
    doi: 10.1086/162827

Rodigas, T. J., Follette, K. B., Weinberger, A., Close, L., & Hines,
    D. C. 2014, ApJL, 791, L37, doi: 10.1088/2041-8205/791/2/L37

Schmidt, T. O. B., Neuhäuser, R., Seifahrt, A., et al. 2008, A&A,
    491, 311, doi: 10.1051/0004-6361:20078840

Schneider, A. C., Windsor, J., Cushing, M. C., Kirkpatrick, J. D.,
    & Wright, E. L. 2016, ApJL, 822, L1,
    doi: 10.3847/2041-8205/822/1/L1

Sivaramakrishnan, A., & Oppenheimer, B. R. 2006, ApJ, 647, 620,
    doi: 10.1086/505192

Smart, R. L., Marocco, F., Sarro, L. M., et al. 2019, MNRAS, 485,
    4423, doi: 10.1093/mnras/stz678

Thalmann, C., Grady, C. A., Goto, M., et al. 2010, ApJL, 718, L87,
    doi: 10.1088/2041-8205/718/2/L87

Tokunaga, A. T., Simons, D. A., & Vacca, W. D. 2002, PASP, 114,
    180, doi: 10.1086/338545

Torres, C. A. O., Quast, G. R., Melo, C. H. F., & Sterzik, M. F.
    2008, Young Nearby Loose Associations, ed. B. Reipurth, 757

Tsuji, T., Ohnaka, K., & Aoki, W. 1996, A&A, 305, L1

Vos, J. M., Allers, K. N., & Biller, B. A. 2017, ApJ, 842, 78,
    doi: 10.3847/1538-4357/aa73cf

Wang, J. J., Ruffio, J.-B., De Rosa, R. J., et al. 2015, pyKLIP: PSF
    Subtraction for Exoplanets and Disks. http://ascl.net/1506.001

Wang, J. J., Rajan, A., Graham, J. R., et al. 2014, in Proc. SPIE,
    Vol. 9147, Ground-based and Airborne Instrumentation for
    Astronomy V, 914755, doi: 10.1117/12.2055753

Wang, J. J., Perrin, M. D., Savransky, D., et al. 2018, Journal of
    Astronomical Telescopes, Instruments, and Systems, 4, 018002,
    doi: 10.1117/1.JATIS.4.1.018002

West, R. A., Karkoschka, E., Friedson, A. J., et al. 1995, Science,
    267, 1296, doi: 10.1126/science.7871426

Witte, S., Helling, C., Barman, T., Heidrich, N., & Hauschildt, P. H.
    2011, A&A, 529, A44, doi: 10.1051/0004-6361/201014105

Witte, S., Helling, C., & Hauschildt, P. H. 2009, A&A, 506, 1367,
    doi: 10.1051/0004-6361/200811501

Wolff, S. G., Perrin, M. D., Maire, J., et al. 2014, in Proc. SPIE,
    Vol. 9147, Ground-based and Airborne Instrumentation for
    Astronomy V, 91477H, doi: 10.1117/12.2055678

Wu, Y.-L., Close, L. M., Males, J. R., et al. 2015, ApJ, 801, 4,
    doi: 10.1088/0004-637X/801/1/4

Yee, J. C., & Jensen, E. L. N. 2010, ApJ, 711, 303,
    doi: 10.1088/0004-637X/711/1/303

Zuckerman, B. 2019, ApJ, 870, 27,
    doi: 10.3847/1538-4357/aaee66

Zuckerman, B., & Song, I. 2004, ApJ, 603, 738,
    doi: 10.1086/381700